Numerical modeling of dynamic frictional rolling contact with an explicit finite element method

Yang, Zhen; Deng, Xiangyun; Li, Zili

DOI
10.1016/j.triboint.2018.08.028

Publication date
2019

Document Version
Final published version

Published in
Tribology International

Tribology International 129 (2019) 214–231

Contents lists available at ScienceDirect

Tribology International

journal homepage: www.elsevier.com/locate/triboint

Numerical modeling of dynamic frictional rolling contact with an explicit finite element method

Zhen Yang, Xiangyun Deng, Zili Li*

Delft University of Technology, Section of Railway Engineering, Stevinweg 1, 2628 CN, Delft, the Netherlands

ARTICLE INFO

Keywords:
Explicit FEM
Frictional rolling
Wheel-rail contact
Dynamic interaction

ABSTRACT

The modeling of dynamic frictional rolling contact is crucial for accurately predicting behavior and deterioration of structures under dynamic interactions such as wheel/rail, tire/road, bearings and gears. However, reliable modeling of dynamic frictional rolling contact is challenging, because it requires a careful treatment of friction and a proper consideration of the dynamic effects of the structures on the contact. This study takes the wheel-rail dynamic interaction as an example to systematically explore the core algorithms for the modeling of dynamic frictional rolling contact by way of explicit finite element analyses. The study also theoretically demonstrates that the explicit finite element method handles nonlinearities in friction, material properties, arbitrary contact geometries and boundary conditions, and fully couples the calculation of frictional rolling contact with the calculation of high-frequency structural dynamics. An indirect validation method for dynamic contact solutions is proposed. To promote the broad use of the method, this paper proposes a detailed procedure for establishing robust wheel-rail dynamic interact tion models and obtaining dynamic contact responses. The proposed procedure can also be applied to the modeling of dynamic interactions occurring to tire-road, bearings and gears.

1. Introduction

The problem of rolling contact is nonlinear in many aspects [1]. The modeling of dynamic rolling contact is crucial for accurately predicting behavior and deterioration of structures under dynamic interactions such as wheel/rail, tire/road, bearings and gears. A reliable dynamic rolling contact model requires a careful treatment of nonlinear frictional rolling contact and a proper consideration of the dynamic effects of the structures on the contact. Since the wheel-rail interaction due to the frictional rolling contact significantly influences the vehicle dynamics and stability [2] and the dynamic effects involved in wheel-rail interactions can be increased by high-speed rolling, a systematic study of wheel-rail dynamic interactions is highly desired, especially within the context of booming high-speed railways. This study thus takes the wheel-rail dynamic interaction as an example to systematically explore the core procedure dedicated to the modeling of dynamic frictional rolling contact .

Studies on wheel-rail contact date from the 19th century. Hertz [3] was among the earliest researchers to provide an analytical solution to frictionless normal contact between elastic bodies with a half-space assumption. Mindlin [4] developed the Hertz contact theory to treat shifts of contact bodies by a tangential force within its friction limit. Wheel-rail friction rolling contact was first studied by Carter [5], who calculated creepage in the rolling direction with a 2D analytical model. Vermeulen and Johnson [6] then extended Carter's 2D theory to 3D with pure creepage and without spin by assuming an elliptical adhesion area.

With the development of the computer and computational sciences, numerical methods have increasingly been employed in the study of wheel-rail contact, and these methods are believed to be more appropriate for solving wheel-rail rolling with high complexity in contact conditions and material properties [7]. The numerical methods may be divided into two classes [8]: the boundary element method (BEM) for local analyses based on the half-space and quasi-quarter-space [9] assumptions and the finite element method (FEM) for global analyses based on general continuum mechanics. Important contributions to the BEM solutions of wheel-rail frictional rolling contact with arbitrary creepages and spin were made by Kalker [10], whose simplified and full theories have been implemented in the extensively used computer programs FASTSIM and CONTACT, respectively. Since the BEM-based approaches discretize the surfaces of contact bodies in only the limited domain of potential contact areas, they are restricted to linear elastic contact problems [1] and fail to consider the wheel/rail dynamic effects related to contact even in non-steady state contact solutions [8]. Here, the wheel/rail dynamic effect refers to the fact that the inertia of wheel/rail material elements may influence the stress field because

* Corresponding author.
E-mail address: Z.Li@tudelft.nl (Z. Li).

https://doi.org/10.1016/j.triboint.2018.08.028
Received 25 June 2018; Received in revised form 22 August 2018; Accepted 24 August 2018
Available online 27 August 2018
0301-679X/

these elements “flow” through the deforming region [11] and may play important roles in wheel-rail impact contact and contact-induced unstable vibration [12].

The FEM with a discretization of whole contact bodies has been demonstrated to be a more flexible tool for modeling frictional rolling contact with arbitrary contact geometries, possible material nonlinearities, dissipation and bifurcations and corresponding standing-wave phenomena [13]. Early finite element (FE) wheel-rail contact models have either assumed quasi-static state contact [14–16] or applied contact loads independently calculated by other simplified or multi-body dynamics models [17–19]. Because the inertia of wheel/rail material elements is not involved in the contact calculations, these studies may not consider the dynamic effects related to contact.

The explicit FEM, which has been successfully applied to various nonlinear transient dynamics problems in recent decades [20], has been increasingly proposed for wheel-rail interaction studies. Zhao and Li [21] produced physical contact solutions of wheel-rail friction rolling with the explicit FEM. Wheel-rail contact was rigorously treated and the quasi-steady contact solutions obtained with the explicit FEM corresponded well to those obtained with well-established approaches, i.e., Hertz contact theory and Kalker's CONTACT [10], in both the normal and tangential directions; effect of small geometrical spin was observed. Deng et al. [22] later used explicit FEM to study the wheel-rail frictional rolling contact solutions with large spin. The calculated explicit FE contact solutions have also been shown to be accurate via comparisons with CONTACT solutions. Investigations of wheel-rail contact characteristics using the explicit FEM include the simulations of the transient wheel-rail rolling contact in elastoplasticity [23], in the presence of rail contamination [24], under high and low adhesion conditions [25], as well as with the consideration of velocity-dependent friction [26] and thermal effects [27].

In addition to the studies of wheel-rail contact solutions [21,22] and contact characteristics [23–28], previous studies on wheel-rail interactions with the explicit FEM also include the studies of wheel-rail impact contact (at the rail joint [29–33], squat [34–40], crossing nose [41–46] and crack [47]), studies of flange contact [12,48,49] and track dynamic behavior [39,50,51]. These studies have generally employed algorithm-optimized commercial programs, e.g., ANSYS/LS-DYNA and ABAQUS/Explicit, to efficiently process the large amounts of elements required in the detailed modeling of wheel/track structures and perform time integration with tiny time steps.

To facilitate other researchers to perform simulations of wheel-rail dynamic interactions with those software packages or alternative explicit FEM programs, systematic perceptions of the involved algorithms and modeling knowledge should be provided. Section 2 systematically explores the core algorithms employed in the explicit FE wheel-rail interaction analyses, which represent the mathematical model and numerical solution procedure implemented in the solvers of commercial programs. In addition, this paper theoretically demonstrates that the explicit FEM is a suitable approach for modeling wheel-rail dynamic interactions. The solutions of wheel-rail dynamic interactions provided by the explicit FEM can rarely be directly validated because of the current absence of an experimental method for precisely measuring rolling contact solutions, such as contact stress and strain states, especially under dynamic conditions [47]. Considering that the explicit FEM fully couples the calculation of wheel-rail contact (converted by nodal forces, see Section 4.1) with the calculation of wheel/rail dynamic responses (converted by nodal motions, see Section 4.2), an indirect validation is proposed: the reliability of the wheel-rail dynamic contact solutions may be confirmed by separately verifying the quasi-steady contact solutions and validating the wheel/rail dynamic responses. The former part has been presented in Refs. [21,22] (e.g. Fig. 1 (a)), whereas the abilities of the method to reproduce wheel/track dynamic behavior have been reported in Refs. [31,35,37,43,50,51] (e.g. Fig. 1 (b)).

To promote the broad use of the method, Sections 3 and 4 propose detailed procedures for establishing robust explicit FE wheel-rail dynamic interaction models (pre-processing) and converting outputs into wheel-rail contact and dynamics solutions (post-processing), respectively. The proposed procedure can also be applied to the modeling of dynamic interactions occurring to tire-road, bearings and gears. Section 5 presents a typical numerical example of wheel-rail dynamic interactions to demonstrate the effectiveness of the method. Section 6 presents the concluding remarks and discusses potential improvements in the methodology required to address controversial issues related to wheel-rail dynamic interactions, such as squeal and corrugation. As far as the authors know, this is the first systematic presentation of dynamic frictional rolling contact which combines fundamental theory (mathematical model and numerical solution procedure) with engineering practice. Since the dynamic effects involved in the interactions of contact bodies can be increased with rolling speed and load, this work is expected to benefit future researches of dynamic frictional rolling contact in the context of high-speed railways and heavy-duty bearings.

2. Algorithm of the explicit finite element method

This section systematically explores the core algorithms employed in the explicit FE wheel-rail interaction analyses with a focus on the mathematical model and the numerical solution procedure implemented in the solvers of commercial programs. The reviews of the algorithms are mainly based on the computational mechanics theories illustrated in the literature [20,52–58] and theoretical manuals of commercial explicit FE programs [59–61]. In addition, the applicability of the explicit FEM to wheel-rail dynamic interaction analyses is demonstrated from a theoretical perspective.

In the formulas presented in this paper, we mainly use index notation to represent vectors, matrices and tensors and use bold-faced variables only when the numbers of components and operations are not confusing. We use lowercase subscripts (*i, j, k*) for spatial components, lowercase superscripts (*t*) for time points, capital subscripts (*M*) for hourglass mode numbers, and capital superscripts (*J, M, N*) for nodal/element numbers.

2.1. Mathematical model of wheel-rail dynamic interactions

Lagrangian formulation typically used for transient structural dynamic proble $u_i = u_i(x_k, t) \quad i, k = 1,2,3$ ms is employed for wheel-rail dynamic interaction analyses. When adopting the Lagrangian formulation, the time-dependent displacement u_i in a fixed rectangular Cartesian coordinate system can be expressed in terms of the convected coordinates x_k in the same coordinate system and time t as follows:

$$u_i = u_i(x_k, t) \quad i, k = 1,2,3 \tag{1}$$

A general 3D transient structural dynamics problem may then be described by constrained partial difference governing equations as follows:

Momentum conservation equations:

$$\sigma_{ij,j} + \rho f_i = \rho \ddot{u}_i \qquad \text{in } \Omega \;\; i, j = 1,2,3 \tag{2a}$$

Displacement boundary conditions:

$$u_i = D_i \qquad \text{on } \Gamma_u \tag{2b}$$

Traction boundary conditions:

$$\sigma_{ij} n_j = T_i \qquad \text{on } \Gamma_s \tag{2c}$$

Contact discontinuity conditions:

$$(\sigma_{ij}^{+} - \sigma_{ij}^{-}) n_i = 0 \qquad \text{on } \Gamma_c \tag{2d}$$

Initial conditions:

$$u_i(x_k, 0) = U_i(x_k), \;\; \dot{u}_i(x_k, 0) = V_i(x_k) \;\; \text{in } \Omega \tag{2e}$$

Material constitutive relation:

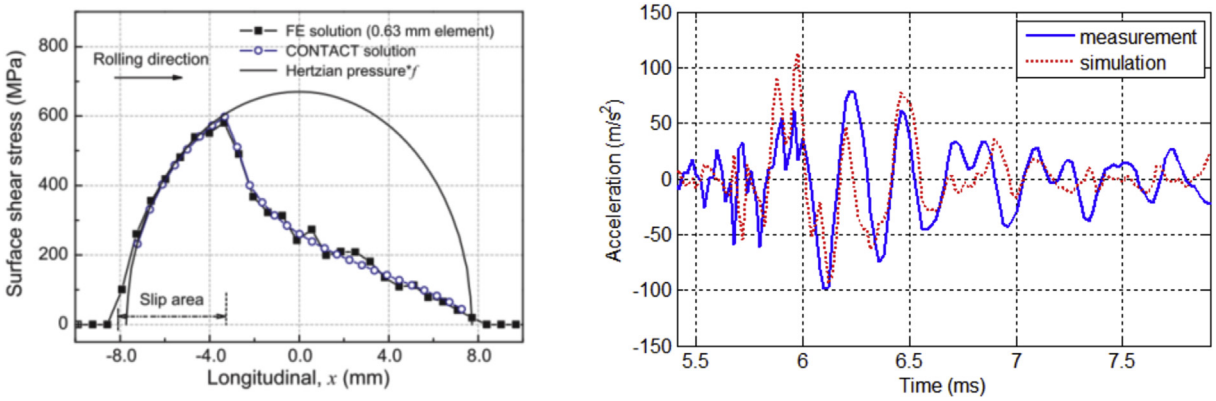

(a) contact solution [21] (b) hammer-excited rail vibration [31]

Fig. 1. Direct verification and validation of the numerical results obtained with explicit FEM. (a) contact solution [21] (b) hammer-excited rail vibration [31].

$$\dot{\sigma}_{ij} = \dot{\sigma}_{ij}(E, v, E_t, x_i, u_i, \dot{\varepsilon}_{ij}, \ldots) \tag{2f}$$

Strain-displacement relation:

$$\dot{\varepsilon}_{ij} = (\dot{u}_{i,j} + \dot{u}_{j,i})/2 \tag{2g}$$

where σ_{ij} is Cauchy stress tensor; ρ is the current density; f_i is the body force density; D_i is the prescribed displacement boundary conditions on part of the boundary Γ_u; T_i represents the components of the traction boundary conditions on part of the boundary Γ_s; n_i is a unit outwardly normal to a boundary element on Γ; U_i and V_i are the initial displacements and velocities, respectively; and E, v and E_t are the Young's modulus, Poisson's ratio and tangent modulus of the material, respectively. The rate form adopted in Eqns. (2f) and (2g) may take nonlinearities into account.

The displacement-based FEM (compared with the force-based FEM) is employed to solve the dynamic problem described in Eqn. (2). By removing all displacement constraints and assuming that the reactions are known, the variational governing equation can be derived by Hamilton's principle as follows:

$$\int_\Omega (\rho\ddot{u}_i - \sigma_{ij,j} - \rho f_i)\delta u_i d\Omega + \int_{\Gamma_s} (\sigma_{ij}n_j - T_i)\delta u_i d\Gamma + \int_{\Gamma_c} (\sigma_{ij}^+ - \sigma_{ij}^-)n_j\delta u_i d\Gamma = 0 \tag{3}$$

Eqn. (3) is a statement of the principle of virtual work, in which δu_i is the variation of displacement. By applying the Gauss divergence theorem to convert the surface integral to the volume integral, the following is obtained:

$$\int_\Omega (\sigma_{ij}\delta u_i)_{,j}\, d\Omega = \int_{\Gamma_s} (\sigma_{ij}n_j)\delta u_i ds + \int_{\Gamma_c} (\sigma_{ij}^+ - \sigma_{ij}^-)n_j\delta u_i d\Gamma \tag{4}$$

Noting the mathematical identity:

$$(\sigma_{ij}\delta u_i)_{,j} = \sigma_{ij,j}\delta u_i + \sigma_{ij}\delta u_{i,j} \tag{5}$$

Then, the weak form of the equilibrium equation can be derived as follows:

$$\int_\Omega \rho\ddot{u}_i\delta u_i d\Omega + \int_\Omega \sigma_{ij}\delta u_{i,j} d\Omega = \int_\Omega \rho f_i\delta u_i d\Omega + \int_{\Gamma_s} T_i\delta u_i d\Gamma \tag{6}$$

To solve Eqn. (6) numerically, a spatial discretization may be used to express the equilibrium equation in terms of time-dependent nodal unknowns and base functions. A mesh of finite elements interconnected at nodal points on the reference configuration is thus superimposed, and particles are tracked through time:

$$u_i = u_i(x_k(\xi, \eta, \zeta), t) = \sum_{N=1}^{n} \varphi^N(\xi, \eta, \zeta)u_i^N(t) \qquad i, k = 1,2,3 \tag{7}$$

where φ^N is the shape function in the parametric coordinates (ξ, η, ζ) and n is the number of nodal points defining the element. Summing over all m elements of a FE model, the semi-discrete equation of motion in the matrix notation becomes:

$$\sum_{M=1}^{m} \left(\int_{\Omega_e} \rho \boldsymbol{N}^T\boldsymbol{N}\ddot{\boldsymbol{u}} d\Omega + \int_{\Omega_e} \boldsymbol{B}^T\boldsymbol{\sigma} d\Omega - \int_{\Omega_e} \rho \boldsymbol{N}^T\boldsymbol{f} d\Omega - \int_{\Gamma_{s,e}} \boldsymbol{N}^T\boldsymbol{t} d\Gamma \right)^M = 0 \tag{8}$$

where $\boldsymbol{\sigma}$ is the Cauchy stress vector, and $\boldsymbol{\sigma}^T = (\sigma_{xx}, \sigma_{yy}, \sigma_{zz}, \sigma_{xy}, \sigma_{yz}, \sigma_{zx})$; $\ddot{\boldsymbol{u}}$ is the nodal acceleration vector; $\boldsymbol{N}$ is the shape matrix constructed by the shape functions; $\boldsymbol{B}$ is the strain-displacement matrix containing the first spatial derivatives of the shape functions; and $\boldsymbol{f}$ and $\boldsymbol{t}$ are the prescribed body load vector and traction load vector, respectively. Because the hexahedral solid elements ($n=8$ in Eqn. (7)) are mostly used in explicit FE wheel-rail interaction models, we take them as examples to illustrate the theories summarized in this paper. For the hexahedral elements:

$$\boldsymbol{N}(\xi, \eta, \zeta) = \begin{bmatrix} \varphi^1 & & & \varphi^2 & & & \cdots & & & \varphi^8 & & \\ & \varphi^1 & & & \varphi^2 & & & \cdots & & & \varphi^8 & \\ & & \varphi^1 & & & \varphi^2 & & & \cdots & & & \varphi^8 \end{bmatrix} \tag{8a}$$

$$\varphi^N(\xi, \eta, \zeta) = \frac{1}{8}(1 + \xi\xi^N)(1 + \eta\eta^N)(1 + \zeta\zeta^N) \qquad N = 1,2, \ldots,8 \tag{8b}$$

$$\boldsymbol{B}(\xi, \eta, \zeta) = \begin{bmatrix} \frac{\partial}{\partial x} & & & & & \\ & \frac{\partial}{\partial y} & & & & \\ & & \frac{\partial}{\partial z} & & & \\ \frac{\partial}{\partial y} & \frac{\partial}{\partial x} & & & & \\ & & \frac{\partial}{\partial z} & \frac{\partial}{\partial y} & & \\ \frac{\partial}{\partial z} & & & \frac{\partial}{\partial x} & & \end{bmatrix} \boldsymbol{N}(\xi, \eta, \zeta) \tag{8c}$$

Note that the time dimension in Eqn. (8) is still continuous, and the semi-discrete equation of motion for a general transient structural dynamics problem may thus be rewritten in a shorthand format:

$$\boldsymbol{M}\ddot{\boldsymbol{u}} = \boldsymbol{f}_{\mathbf{ext}} - \boldsymbol{f}_{\mathbf{int}} \tag{9}$$

in which $\boldsymbol{M}$, $\boldsymbol{f}_{\mathbf{int}}$ and $\boldsymbol{f}_{\mathbf{ext}}$ are the mass matrix, internal force vector and external force vector, respectively, and they are defined as follows:

$$\boldsymbol{M} = \sum_{M=1}^{m} \left(\int_{\Omega_e} \rho \boldsymbol{N}^T\boldsymbol{N} d\Omega \right)^M \tag{9a}$$

$$\boldsymbol{f}_{\mathbf{ext}} = \sum_{M=1}^{m} \left(\int_{\Omega_e} \rho \boldsymbol{N}^T \boldsymbol{f} d\Omega + \int_{\Gamma_{s,e}} \boldsymbol{N}^T \boldsymbol{t} d\Gamma \right)^M \tag{9b}$$

$$\boldsymbol{f}_{\mathbf{int}} = \sum_{M=1}^{m} \left(\int_{\Omega_e} \boldsymbol{B}^T \boldsymbol{\sigma} d\Omega \right)^M \tag{9c}$$

By adding two extra terms, $\boldsymbol{f}_{\mathbf{con}}$ and $\boldsymbol{H}$, to the right-hand side of Eqn. (9), the semi-discrete equilibrium equation for the wheel-rail dynamic interaction problem is obtained as follows:

$$\boldsymbol{M}\ddot{\boldsymbol{u}} = \boldsymbol{f}_{\mathbf{ext}} - \boldsymbol{f}_{\mathbf{int}} + \boldsymbol{H} + \boldsymbol{f}_{\mathbf{con}} \tag{10}$$

where $\boldsymbol{H}$ is the anti-hourglass vector that only occurs in the reduced integration to control the zero-energy modes, and $\boldsymbol{f}_{\mathbf{con}}$ is the contact force vector, which can be included as a contribution to the externally applied tractions [20,52]. These two terms will be explicated in Sections 2.5 and 2.6, respectively.

2.2. Numerical solution procedure for the explicit FE wheel-rail dynamic interaction analysis

2.2.1. Time discretization by central difference scheme

Among the various numerical approaches developed for solving the dynamic interaction problem formulated by Eqn. (10), we focus only on the explicit integration scheme using the central difference to approximate the acceleration vector $\ddot{\boldsymbol{u}}$. The explicit schemes calculate the values of dynamic quantities at time step $t + 1$ based entirely on the available values at time step t. Eqn. (10) discretized by the central difference scheme at time step t may be written as follows:

$$\ddot{\boldsymbol{u}}^t = \boldsymbol{M}^{-1}(\boldsymbol{f}_{\mathbf{ext}}{}^t - \boldsymbol{f}_{\mathbf{int}}{}^t + \boldsymbol{H}^t + \boldsymbol{f}_{\mathbf{con}}{}^t) \tag{11}$$

The velocity and displacement vectors may then be obtained using the central difference time integration:

$$\dot{\boldsymbol{u}}^{t+1/2} = \dot{\boldsymbol{u}}^{t-1/2} + \Delta t^{t+1/2} \ddot{\boldsymbol{u}}^t \tag{12a}$$

$$\boldsymbol{u}^{t+1} = \boldsymbol{u}^t + \Delta t^{t+1} \dot{\boldsymbol{u}}^{t+1/2} \tag{12b}$$

where Δt is the time step size, which is constant in the linear analysis but may vary in the nonlinear analysis [52], and

$$\Delta t^{t+1/2} = \frac{\Delta t^{t+1} + \Delta t^t}{2} \tag{13}$$

2.2.2. Procedure for the explicit FE wheel-rail dynamic interaction analyses

The equilibrium Eqn. (11) discretized in both the space and time domains indicates that the numerical solutions of a wheel-rail dynamic interaction problem are dependent on a constant mass matrix and four time-dependent force vectors. Therefore, the numerical solution procedure for the explicit FE wheel-rail dynamic interaction analysis is mainly composed of mass matrix and force vector calculations. A lumped mass matrix can be constructed by a row summation scheme [62] prior to the iteration to promote the efficiency and practicality of the explicit FEM. For the force vectors, the external force vector $\boldsymbol{f}_{\mathbf{ext}}$ may be calculated directly by the given load conditions (see Section 2.3); the internal force vector $\boldsymbol{f}_{\mathbf{int}}$ contributed by stresses may be calculated by the constitutive and strain-displacement formulations built in the element and material models (see Section 2.4); and the anti-hourglass force vector $\boldsymbol{H}$ and the contact force vector $\boldsymbol{f}_{\mathbf{con}}$ may be calculated by the Flanagan-Belytschko scheme [63] (see Section 2.5) and penalty contact method [55] (see Section 2.6), respectively. Table 1 outlines a numerical procedure for the explicit FE wheel-rail dynamic interaction analysis. This procedure has been implemented in commercial explicit FE programs and used in previous wheel-rail contact and dynamics studies, although variations are possible, e.g., processing contact with a “predictor-corrector method” [58,64]: 1. Predict nodal accelerations/velocities/displacements before step (d) in Table 1 by assuming no contact occurs; 2. Check the contact conditions in step (d) with the predicted displacement field; and 3. Enforce contact forces and correct the nodal motions, i.e., the acceleration, velocity and displacement.

The numerical solution procedure presented in Table 1 contains two loops. The outer loop is constructed mainly by formulating the equation of motion and solving the equation with the central difference scheme, whereas the inner loop calculates the wheel-rail contact, which is called as a subroutine at each time step prior to the updates of the structural dynamic responses. The calculation of wheel/rail dynamics and the calculation of wheel-rail contact are, therefore, coupled in the numerical algorithm, which provides the theoretical basis for the indirect validation of the wheel-rail dynamic interaction solutions mentioned in Section 1.

2.2.3. Stability of integration

The explicit integration scheme has a simple and neat solution procedure but is conditionally stable: the integration is only stable if the time step size used is smaller than the critical time step size. The Courant-Friedrichs-Lewy stability condition [65] can be used to guarantee convergence, which requires that a sound wave may not cross the smallest element within one time step:

$$\Delta t_c \leq L_c / C_d \tag{14}$$

where Δt_c is the critical time step size; L_c is the shortest characteristic dimension of the element; and C_d is the dilatational wave speed of the material. For hexahedral elements:

$$L_c = V_e / A_{emax} \tag{14a}$$

where V_e is the element volume, and A_{emax} is the largest surface area. For elastic materials [59]:

$$C_d = \sqrt{E(1-\nu)/[(1+\nu)(1-2\nu)\rho]} \tag{14b}$$

Eqn. (14b) can be simplified for one-dimensional solids where the Poisson's ratio is neglected, i.e.:

$$\boldsymbol{C_d} = \sqrt{\boldsymbol{E/\rho}} \tag{14c}$$

In the calculation of wheel-rail interactions, the wheel and rail are generally considered to be steel with nominal values of $E = 210$ GPa, $\nu = 0.3$ and $\rho = 7800$ kg/m^3; thus, C_d is equal to approximately 6 km/s. The critical time step Δt_c characterized in inequality (14) may vary in nonlinear dynamic analyses because of changes in the material parameters and/or geometry. The time step Δt should be correspondingly adjusted in a conservative manner so that the condition in inequality (14) is satisfied with certainty at all time steps. To guarantee the stability and simultaneously decrease the solution time, a suitable scale factor sf may be employed to control the time step, i.e., $\Delta t = sf \times L_c / C_d$. A detailed discussion about the scale factor sf used in the wheel-rail dynamic interaction analysis is given in Section 3.3.6.

Because the numerically obtained highest natural frequency of a structure is bounded by the highest frequency of any individual element in the FE discretization [59], as long as the elements and time steps are sufficiently small, an explicit FE model may include in its solution all the relevant vibration modes of structures and continua and associated wave propagations [23]. In addition, small time step sizes can reduce the truncation errors but increase the round-off errors. By adding displacement increments to the initial geometries:

$$\boldsymbol{x}^t = \boldsymbol{x}^0 + \boldsymbol{u}^t \tag{15}$$

in the geometry updating step (step (j) in Table 1), rather than to the geometries obtained at the previous time step, solutions turn out to be much less sensitive to the round-off errors [59].

2.3. External force

The external force vector in Eqn. (11) can be directly constructed by

Table 1
Numerical procedure for the explicit FE wheel-rail dynamic interaction analysis.

Initialize algorithm:

- Apply initial conditions U_i and V_i (by Eqn. (2e));
- Set $\dot{\boldsymbol{u}}^{-1/2} = \dot{\boldsymbol{u}}^0 = \dot{u}_i(x_k, 0) = V_i(x_k)$ and $\Delta t^0 = 0$;
- Define the slave/master nodes/segments for wheel-rail contact pairs;
- Construct the lumped mass matrix $\boldsymbol{M}$;
- Set the termination time: T_{ter}.

LOOP1 t =0, 2,…, n (time step number)

(a) Apply load conditions to construct the external force vector $\boldsymbol{f}_{\mathbf{ext}}{}^t$ (see Section 2.3);

(b) Process elements to construct the internal force vector $\boldsymbol{f}_{\mathbf{int}}{}^t$ (see Section 2.4);

(c) Construct the anti-hourglass vector $\boldsymbol{H}^t$ (see Section 2.5);

(d) Construct the wheel-rail contact force vector $\boldsymbol{f}_{\mathbf{con}}{}^t$ (see Section 2.6);

LOOP2 N=1, 2,…, m (slave wheel node number)

I. Locate the corresponding master segment on the rail for slave wheel node N;

II. Locate the wheel-rail contact point (projection of the slave node on the master segment);

III. Check for penetration;

IF penetration occurs,

i. Calculate the normal contact forces $\boldsymbol{f}_{cN}{}^t$;

ii. Calculate the tangential contact forces $\boldsymbol{f}_{cT}{}^t$;

END IF

END LOOP2

(e) Update time step size Δt^{t+1} to prevent unstable contact or integration (see Section 2.2.3);

(f) Update nodal accelerations $\ddot{\boldsymbol{u}}^t$ (by Eqn. (11));

(g) Impose displacement constraints (see Section 2.7);

(h) Update nodal velocities $\dot{\boldsymbol{u}}^{t+1/2}$ (by Eqn. (12a));

(i) Update nodal displacements $\boldsymbol{u}^{t+1}$ (by Eqn. (12b));

(j) Update structural geometries (by Eqn. (15));

(k) Update time $\sum_{t+1} \Delta t$ and check for termination: **IF** $\sum_{t+1} \Delta t \geq T_{ter}$ → STOP

END LOOP1

Output: wheel/rail nodal force and nodal motion ($\ddot{\boldsymbol{u}}$, $\dot{\boldsymbol{u}}$ and $\boldsymbol{u}$)

the prescribed load conditions. Common external loads applied to wheel-rail dynamics and contact models include gravitational loads, hammer impulse loads and driving torques. The first two may be regarded as the body forces and surface nodal loads contributing to the first and second terms of Eqn. (9b), respectively. The driving torque is discussed in Section 3.3.3.

2.3.1. Gravitational load

Gravitational loads are generally applied to wheel-rail interaction models to initialize internal forces before proceeding with calculations of dynamic responses. The gravitational loads are applied as body forces by setting a fixed gravitational acceleration g as follows:

$$\boldsymbol{f}_{\mathbf{grav}} = \sum_{M=1}^{m} \left(\int_{\Omega_e} \rho \boldsymbol{N}^T \boldsymbol{f} d\Omega \right)^M = \sum_{M=1}^{m} \left(\int_{\Omega_e} \rho \boldsymbol{N}^T \boldsymbol{N} g d\Omega \right)^M = \boldsymbol{M} g \tag{16}$$

2.3.2. Hammer impulse

Hammer impulses may be applied to the explicit FE wheel/track models as surface nodal loads to characterize the dynamic behavior of structures [50,51]. The prescribed surface nodal loads The prescribed surface nodal loadat the Nth node of a surface segment p^N may be converted to the traction boundary conditions as follows:

Table 2
Hourglass base vectors for hexahedral elements.

Node (N)	Γ_1^N	Γ_2^N	Γ_3^N	Γ_4^N
1	1	1	1	−1
2	1	−1	−1	1
3	−1	−1	1	−1
4	−1	1	−1	1
5	−1	−1	1	1
6	−1	1	−1	−1
7	1	1	1	1
8	1	−1	−1	−1

Note that the hourglass shape vectors γ_M^N are orthogonal to the linear velocity field $\dot{\boldsymbol{u}}_{\mathrm{LIN}}^N$, which makes the anti-hourglass force vector f_{iM}^N also orthogonal to the linear velocity field $\dot{\boldsymbol{u}}_{\mathrm{LIN}}^N$ and is necessary for accurately detecting an hourglass. Therefore, the hourglass control scheme avoids transferring energy to or from the rigid body and uniform strain modes.

$$\boldsymbol{t} = t_i(\xi,\eta) = n_i \sum_{N=1}^{4} \varphi^N(\xi,\eta) p^N \qquad \mathrm{i}=1,2,3 \tag{17}$$

where n_i is the unit normal vector to the surface segment; see Eqn. (26b) in Section 2.6.1. A Gaussian one-point quadrature may then be used to conduct the surface integration in Eqn. (9b) as follows:

$$\int_{\Gamma_{s,e}} \boldsymbol{N}^T \boldsymbol{t} d\Gamma = \int_{-1}^{1}\int_{-1}^{1} \boldsymbol{N}^T \boldsymbol{t}(\xi,\eta)|\boldsymbol{J}| d\xi d\eta = 4\boldsymbol{N}^T \boldsymbol{t}(0,0)\,|\boldsymbol{J}(0,0)| \tag{18}$$

in which $\boldsymbol{J}$ is the surface Jacobian matrix and $4|\boldsymbol{J}(0,0)|$ approximates the element surface.

2.4. Internal force

To construct the internal force vector given in Eqn. (9c), the strain-displacement matrix $\boldsymbol{B}$ and the stress vector $\boldsymbol{\sigma}$ are required. Continuing to take the hexahedral element as examples, the Jacobian matrix $\boldsymbol{J}$ is used to relate the displacement in the parametric coordinate system to the global coordinates system:

$$\begin{bmatrix} \frac{\partial \varphi^N}{\partial x} \\ \frac{\partial \varphi^N}{\partial y} \\ \frac{\partial \varphi^N}{\partial z} \end{bmatrix} = \boldsymbol{J}^{-1} \begin{bmatrix} \frac{\partial \varphi^N}{\partial \xi} \\ \frac{\partial \varphi^N}{\partial \eta} \\ \frac{\partial \varphi^N}{\partial \zeta} \end{bmatrix} \qquad N = 1,2,\ ...,8 \tag{19}$$

The strain-displacement matrix $\boldsymbol{B}$ may then be obtained with Eqn. (8c), and the strain rate $\dot{\boldsymbol{\varepsilon}}$ and stress rate $\dot{\boldsymbol{\sigma}}$ are readily calculated by applying the strain-displacement relation and the material constitutive relation in Eqns. (2g) and (2f), respectively. The material constitutive relation expressed in Eqn. (2f) can be either linear or nonlinear. See Ref. [20] for an additional discussion of the material constitutive relations. The Cauchy stresses may be calculated using explicit time integration as follows:

$$\boldsymbol{\sigma}(t+\Delta t) = \boldsymbol{\sigma}(t) + \dot{\boldsymbol{\sigma}}\Delta t \tag{20}$$

Because $\boldsymbol{G}(\xi,\eta,\zeta) = \boldsymbol{B}^T\boldsymbol{\sigma}$ is defined over the volume, the internal forces of structures may be updated with a Gaussian one-point quadrature analogous to Eqn. (18) as follows:

$$\int_{\Omega_e} \boldsymbol{G}(\xi,\eta,\zeta) d\Omega = 8\boldsymbol{G}(0,0,0)\,|\boldsymbol{J}(0,0,0)| \tag{21}$$

in which $8|\boldsymbol{J}(0,0,0)|$ approximates the element volume.

2.5. Hourglass control

Explicit FE wheel-rail interaction analyses have generally adopted the one-point quadrature scheme (Eqn. (18) and (21)) for the sake of computational efficiency, which may also avoid the shear locking issue. The one-point reduced integration, however, leads to spurious zero-energy modes or "hourglass" modes for hexahedral and quadrilateral elements. For hexahedral elements, the hourglass modes are present whenever diagonally opposite nodes have identical velocities, which give zero strain rates according to Eqn. (2g). The anti-hourglass force vector $\boldsymbol{H}$ is thus introduced in Eqn. (10) to avoid the undesirable hourglass modes from growing large and destroying solutions. An orthogonal Flanagan-Belytschko hourglass control scheme [63] may be used in the explicit FE wheel-rail dynamic interaction analysis. The anti-hourglass forces are given by:

$$\boldsymbol{H} = f_{iM}^N = \frac{1}{4} Q_{hg} \rho C_d V_e^{\frac{2}{3}} \sum_{N=1}^{8} \left(\dot{u}_i \gamma_M\right)^N \gamma_M^N \qquad i = 1,2,3;\ M = 1,2,3,4 \tag{22}$$

where Q_{hg} is the hourglass coefficient, and the nodal velocities $\dot{u}_i^N$ are the sum of the hourglass field $\dot{\boldsymbol{u}}_{\mathrm{HG}}^N$ and the linear portion of the nodal velocities $\dot{\boldsymbol{u}}_{\mathrm{LIN}}^N$:

$$\dot{u}_i^N = \dot{\boldsymbol{u}}^N = \dot{\boldsymbol{u}}_{\mathrm{HG}}^N + \dot{\boldsymbol{u}}_{\mathrm{LIN}}^N \tag{22a}$$

The hourglass shape vectors γ_M^N are defined in terms of the hourglass base vectors Γ_M^N given in Table 2:

$$\gamma_M^N = \Gamma_M^N - \varphi_i^N \sum_{N=1}^{8} \dot{u}_i^N \Gamma_M^N \tag{22b}$$

Flanagan-Belytschko hourglass control scheme given by Eqn. (22) is in viscous form: the calculated anti-hourglass force is proportional to the components of the nodal velocity contributing to hourglass modes. This method is more suitable for dynamic problems with high velocity/strain rate. In contrast, the stiffness-form hourglass control scheme calculates the anti-hourglass forces proportional to the components of the nodal displacement contributing to hourglass modes. The stiffness-form scheme can reduce total accumulated hourglass deformation and is preferred for low rate problems. In addition to Flanagan-Belytschko scheme, other hourglass control methods such as Belytschko-Bindeman [66], Puso [67] and Jabareen-Rubin [68] have also been implemented in the explicit FE commercial programs [59,60]. To estimate the effects of different hourglass control schemes, the ratio of the hourglass energy (i.e. the work done by the anti-hourglass force) over the internal energy may be checked. As a general guideline, the hourglass energy should not exceed 10% of the internal energy.

2.6. Contact algorithm

Because of its iterative nature [20,52], the penalty contact algorithm is considered to be suitable for solving explicit FE contact problems and has been broadly proposed to enforce the wheel-rail contact constraints. As indicated in Table 1, the penalty contact algorithm can be straightforwardly implemented in the explicit FE programs as a subroutine. Penetration is allowed and represents the key to the penalty method [20]. The penalty algorithm checks each slave node for penetration through the master surface. **The contact surface with coarser mesh or with stiffness higher than its counterpart is usually treated as the master surface.** This study refers to the wheel surface as the slave surface and to the rail surface as the master surface; the symmetry of the approach eliminates any bias in this choice [59].

2.6.1. Normal contact

In a wheel-rail contact simulation, a slave wheel node is seldom in exact contact with a master rail node. Instead, the slave wheel node usually "contacts" a segment composed of four rail surface nodes. At each time step, the contact segments on the rail surface need to be searched for. For an arbitrary slave node N_s defined on the prospective wheel contact surface, we need first locate the closest master node and segment on the rail surface. As shown schematically in Fig. 2 (a), the

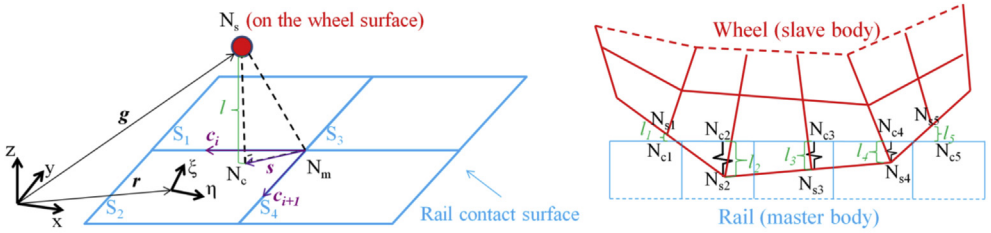

Fig. 2. Parametric representation of wheel-rail contact.

slave node N_s is denoted as a red spot, and its closest master node N_m is stored by segments S_i (i = 1,2,3,4). If the nodes N_s and N_m do not coincide, N_s can be shown to lie in one of the segments S_i via the following tests:

$$(\boldsymbol{c}_i \times \boldsymbol{s})\cdot(\boldsymbol{c}_i \times \boldsymbol{c}_{i+1}) > 0 \ , \ (\boldsymbol{c}_i \times \boldsymbol{s})\cdot(\boldsymbol{s} \times \boldsymbol{c}_{i+1}) > 0 \qquad i = 1,2,3,4 \tag{23}$$

The vectors $\boldsymbol{c}_i$ and $\boldsymbol{c}_{i+1}$ are along the edges of S_i and point outwards from N_m, and the vector $\boldsymbol{s}$ is the projection of the vector beginning at N_m and ending at N_s onto the closest segment (S_2 in this demonstration). The inequalities of Eqn. (23) ensure that the vector $\boldsymbol{s}$ is between the vectors $\boldsymbol{c}_i$ and $\boldsymbol{c}_{i+1}$ and is thus located within the segment S_i. If the inequalities are not satisfied, another master segment containing N_m will be checked. The algorithm does not limit the number of segments containing N_m, and the master segment determined at the previous time step is preferentially checked at each time step.

The "contact point" N_c is the projection of the slave wheel node N_s on the master rail segment (S_2 in this demonstration). The determined master segment has a bilinear parametric representation in a local coordinate system as follows:

$$\boldsymbol{r}(\xi, \eta) = \sum_{i=1}^{3} f_i(\xi, \eta)\boldsymbol{i}_i \tag{24}$$

$$f_i(\xi, \eta) = \sum_{N=1}^{4} \varphi^N(\xi, \eta)x_i^N \qquad i = 1,2,3 \tag{24a}$$

$$\varphi^N(\xi, \eta) = \frac{1}{4}(1 + \xi\xi^N)(1 + \eta\eta^N) \quad N = 1,2, \ ...,4 \tag{24b}$$

where $\boldsymbol{r}(\xi, \eta)$ represents the master segment; $\boldsymbol{i}_i$ represents unit direction vectors; and x_i^N represents the nodal coordinates of the nodes contained by the segment. Let $\boldsymbol{g}$ be a vector drawn to the slave node N_s. The contact point N_c with coordinates (ξ_c, η_c) on the master segment can be determined by satisfying the following:

$$\frac{\partial \boldsymbol{r}}{\partial \xi}(\xi_c, \eta_c)\cdot[\boldsymbol{g} - \boldsymbol{r}(\xi_c, \eta_c)] = 0 \tag{25a}$$

$$\frac{\partial \boldsymbol{r}}{\partial \eta}(\xi_c, \eta_c)\cdot[\boldsymbol{g} - \boldsymbol{r}(\xi_c, \eta_c)] = 0 \tag{25b}$$

The coordinates (ξ_c, η_c) in Eqns. (25a) and (25b) may be solved numerically with Newton-Rapson iterations. Since the method may diverge with distorted elements [59], a careful treatment of mesh in the wheel-rail contact region, especially in the solution zone, is highly desirable. Penetration of the slave wheel node through its master rail segment may then be judged by a scalar l:

$$l = \boldsymbol{n}\cdot[\boldsymbol{g} - \boldsymbol{r}(\xi_c, \eta_c)] \tag{26a}$$

$$\boldsymbol{n} = n_i(\xi_c, \eta_c) = \left(\frac{\partial \boldsymbol{r}}{\partial \xi} \times \frac{\partial \boldsymbol{r}}{\partial \eta}\right) \Big/ \left|\frac{\partial \boldsymbol{r}}{\partial \xi} \times \frac{\partial \boldsymbol{r}}{\partial \eta}\right| \tag{26b}$$

If $l \geq 0$, no penetration occurs and nothing will be done; if $l < 0$, an interface force vector $\boldsymbol{f}_{cN}$ normal to the master segment will be applied to the contact point, and its magnitude is proportional to the amount of penetration:

$$\boldsymbol{f}_{cN} = -lk\boldsymbol{n} \tag{26c}$$

Hence, interface springs may be assumed between the penetrating slave wheel nodes and rail contact surface as shown in Fig. 2 (b), and the penalty contact (spring) stiffness k is intrinsically the combination of a geometrical penalty term and a velocity penalty term [58]. For the hexahedral elements containing the master segments used in the wheel-rail contact surfaces, k may be given in terms of the bulk modulus K, the element volume V and the face area A as follows:

$$k = \frac{f_{SI}KA^2}{V} \tag{26d}$$

where f_{SI} is a scale factor for the penalty contact stiffness. The choice of its value in wheel-rail interaction simulations will be discussed in Section 3.3.1. The equal and opposite contact forces distributed over the master segment nodes $\boldsymbol{f}_{master}^J$ may also be obtained as follows:

$$\boldsymbol{f}_{master}^J = -\varphi^J(\xi_c, \eta_c)\boldsymbol{f}_{cN} \qquad J = 1,2,3,4 \tag{27}$$

The penalty contact algorithm implemented in the explicit FEM can treat an arbitrarily shaped surface by representing the surface with a faceted mesh.

2.6.2. Tangential contact

The Coulomb friction law is available to solve the wheel-rail tangential contact. A trial tangential contact nodal force $\boldsymbol{f}^*$ at time step $t + 1$ may be defined as follows:

$$\boldsymbol{f}^* = f_{cT}^t - k\Delta\boldsymbol{e} \tag{28a}$$

where $\boldsymbol{f}_{cT}{}^t$ is the tangential contact force calculated at time step t; k is the penalty contact stiffness; and $\Delta\boldsymbol{e}$ is the incremental movement of the slave wheel node along the rail surface:

$$\Delta\boldsymbol{e} = \boldsymbol{r}^{t+1}(\xi_c^{t+1}, \eta_c^{t+1}) - \boldsymbol{r}^{t+1}(\xi_c^t, \eta_c^t) \tag{28b}$$

The traction bound $f_{bound}{}^t$ at time step t in the Coulomb friction law is the product of the magnitude of the normal force $\boldsymbol{f}_{cN}{}^t$ at the same time step and the coefficient of friction (COF) μ:

$$f_{bound}{}^t = \mu|\boldsymbol{f}_{cN}{}^t| \tag{28c}$$

The tangential contact force at time step $t + 1$ may thus be written as follows:

$$f_{cT}^{t+1} = \begin{cases} \boldsymbol{f}^* & if \ |\boldsymbol{f}^*| \leq f_{bound}^{t+1} \\ \frac{\boldsymbol{f}^*}{|\boldsymbol{f}^*|} & if \ |\boldsymbol{f}^*| > f_{bound}^{t+1} \end{cases} \tag{28d}$$

The COF μ, which is considered a constant in the classical Coulomb's law, may vary with various factors in wheel-rail contact such as sliding speed, contact pressure, surface lubrication or contamination, roughness, temperature, and humidity [26]. Section 2.2.2 demonstrated that the explicit FEM couples the calculation of wheel/rail dynamic responses with the calculation of wheel-rail contact in the time domain. Thus, a velocity-dependent Coulomb's law with a functional COF may be implemented in the explicit FEM. The COF updated at each time step

may be expressed in terms of the static and dynamic friction coefficients μ_s and μ_d, respectively, a decay constant c and wheel-rail relative sliding velocities $\dot{\boldsymbol{u}}_{rel}$ between the slave nodes and master segments at the same time step as follows:

$$\mu = \mu_d + (\mu_s - \mu_d)e^{-c|\dot{\boldsymbol{u}}_{rel}|} \tag{29a}$$

$$\dot{\boldsymbol{u}}_{rel} = \Delta \boldsymbol{e}/\Delta t \tag{29b}$$

The decay constant c describes how fast the static coefficient approaches the dynamic coefficient and may be determined by fitting the measured results [26]. Because the wheel-rail contact forces can be physically interpreted as externally applied tractions [20,52], the contact force vector required in Eqn. (11) may be expressed as follows:

$$\boldsymbol{f}_{\mathbf{con}}^{t} = \sum_{M=1}^{m} \left(\int_{\Gamma_{c,e}} \boldsymbol{N}^T (f_{cN}^{t} + f_{cN}^{t}) d\Gamma \right)^M \tag{30}$$

The traditional division of an elastic contact problem into a normal problem and a tangential problem is based on an assumption that the friction transmitted between elastic contact bodies has a negligible influence on the normal contact solutions [69]. In the explicit FEM, the normal and tangential contacts are calculated successively and dependently at each time step, which is necessary for solving inelastic contact problems. Studies with the explicit FEM [22,23] have indicated that the tangential elastoplastic wheel-rail contact solutions have noticeable effects on the normal solutions: an increase in tangential force increases plastic flow, and the contact patch tends to become larger in size and shifts forward more.

2.6.3. Contact stability

The contact-based critical time step determined by the penalty contact algorithm is proportional to $\min\left\{\sqrt{\frac{m^J}{k}}\right\}$, where m^J $(J = 1,2)$ is essentially the mass attached to the contact "spring" and k is the penalty contact stiffness given in Eqn. (26d). The time step size Δt used in the explicit FEM should not exceed the contact-based critical time step to avoid contact instability. The easiest method of increasing the contact-based critical time step is to scale down the penalty contact stiffness k.

2.7. Displacement constraints

Suitable displacement constraints are necessarily defined as essential boundary conditions in the mathematical model of wheel-rail dynamic interactions and are largely applied to structural boundaries, such as the inner end of wheel half-axles, the rail ends and the rail bottom surfaces (see Section 3.3.4). These constraints can be imposed by setting the constrained acceleration components to zero [59]. Since the prescribed nodal displacement constraints are imposed in the local coordinate system, an orthogonal matrix Q constructed by the normalized unit vectors in the local axes needs to be employed to transform the global nodal acceleration vectors $\ddot{u}_i^N$ (for node N) updated by Eqn. (11) to the local system as follows:

$$\ddot{u}_{LOCi}^N = Q\ddot{u}_i^N \qquad i = 1,2,3 \tag{31a}$$

After the constrained acceleration components are zeroed, the modified vectors $\ddot{u}_{LOCi}^N$ can be transformed back to the global system:

$$\ddot{u}_i^N = Q^T\ddot{u}_{LOCi}^N \qquad i = 1,2,3 \tag{31b}$$

where $\ddot{u}_i$ in Eqn. (31b) is the finally updated nodal acceleration vector of the time step, which will further be integrated to approximate the nodal velocities and displacements by Eqns. (12a) and (12b).

2.8. Summary of the algorithms

By systematically exploring the core algorithms employed in the explicit FE wheel-rail interaction analyses, this section enhances the understanding of the explicit FE wheel-rail interaction studies and shows the applicability of the explicit FEM to the wheel-rail dynamic interaction analyses from a theoretical perspective. The advantages of using the explicit FE algorithm to solve the wheel-rail dynamic interactions may thus be summarized as follows:

- The explicit FEM couples the calculation of wheel/rail structural dynamic responses with the calculation of wheel-rail contact, which makes the explicit FEM a suitable approach for solving wheel-rail dynamic interactions and provides a theoretical basis for the indirect validation of the wheel-rail dynamic contact solution.
- The explicit FEM is capable of treating nonlinearities in materials, geometry and boundary conditions. The implemented penalty contact algorithm can handle arbitrarily shaped contact surfaces, and it calculates normal and tangential contact successively and dependently at each time step, which is necessary for solving inelastic wheel-rail contact problems.
- By avoiding the need for matrix evaluation, assembly and decomposition as required by implicit integration algorithms, the explicit procedure is computationally attractive for analyzing high-frequency dynamic problems of short duration, especially when the total dynamic response time that must be modeled is only a few orders of magnitude longer than the stability critical time step, which is frequently the case in wave propagation analyses [70]. The explicit wheel-rail FE model may include in its solution all the relevant vibration modes of structures and continua and associated wave propagations.

The conditionally stable explicit FEM is, however, less efficient than the implicit FEM for static equilibrium analyses or low-frequency dynamics problems lasting for a much longer time period [47]. Implicit-explicit sequential approaches may thus be employed to minimize both the solution time and the dynamic effects induced by the initialization of wheel-rail interaction analysis. The implicit-explicit sequential approach involves performing an implicit static equilibrium analysis followed by an explicit transient dynamics analysis. The modeling procedure is elaborated in the next section.

3. Modeling procedure

This section discusses how to establish robust explicit FE wheel-rail dynamic interaction models. A basic explicit FE wheel-rail dynamic interaction model may contain a half-track model and a half-wheelset model with its share of the sprung mass of a car body and a bogie. We can divide the modeling procedure into three stages in a physical sequence: Stage 1. build wheel and rail models; Stage 2. let the wheel and rail come into contact and achieve static equilibrium; and Stage 3. let the wheel roll along the rail. The commercial programs ANSYS/LS-DYNA were employed to demonstrate this modeling procedure, and other programs with implementations of implicit-explicit sequential approaches, such as ABAQUS/Explicit, may also be applied.

3.1. Modeling of wheel and rail structures

3.1.1. Geometry modeling

The geometries of wheels and rails, including the contact profiles, should be modeled as realistically as possible because they may influence both the structural dynamic properties and contact solutions. The detailed nominal geometries of a wheel radial section and a rail cross section may initially be created in a graphical software (e.g., AutoCAD; see Fig. 3 (a)). Based on these geometries, the wheel and rail volumes can subsequently be generated in the pre-processing FE software (e.g., ANSYS; see Fig. 3 (b)) by rotating the wheel radial section with respect to the central line of the wheel axle and extruding the rail cross section longitudinally. The wheel/rail volumes are suggested to be generated

(a) Generated in AutoCAD (b) Generated in ANSYS

Fig. 3. Modeling of the wheel and rail geometries. (a) Generated in AutoCAD (b) Generated in ANSYS.

after meshing the wheel radial section and rail cross section for modeling convenience.

3.1.2. Mesh

Adequately fine mesh is needed for a robust FE wheel-rail interaction model, especially when precise contact solutions and high-frequency dynamics are desired. Zhao and Li [21] report that the element size of approximately 1/20 of the minor axis of the contact patch tends to provide accurate contact solutions, whereas approximately 1/10 of the minor axis may be acceptable for many engineering problems. To obtain an optimal mesh in the sense of cost effectiveness and acceptable error, a partially refined mesh as shown in Fig. 4 may yield a better approximate solution [13]. Fine special discretization should be concentrated on the prospective contact regions. Another meshing method balancing the efficiency and accuracy of contact solutions uses the surface-based tie constraints to refine the mesh in the contact regions [42,71]. The tetrahedral or wedge elements with triangular faces, which have indeterminate contact condition at the corners, are not suitable for analyzing contact problems and should be avoided by remeshing the model [60]. In addition, remeshing may be employed to adjust mesh size [21] or the position of solution zone [12] of an explicit FE contact model. Fig. 5 shows the explicit FE model used to study wheel-rail contact transition from single point to two points. Because the contact transition occurs at different rail locations with different prescribed angles of attack (AoA), the position of solution zone is adjusted by remeshing the rail model to capture the contact transition process.

The mesh-determined time step of explicit integration (Eqn. (14)) may be increased by mass scaling, i.e. scale up the mass of a model non-physically, to reduce simulation time. One simple method of the mass scaling is to artificially increase the material density (Eqn. (14b)). Note that the mass scaling is only justifiable when it has insignificant influence on the solution, which is usually the case for quasi-static analyses. For dynamic analyses where an accurate mass distribution is critical to the solution, the added penetrations and kinetic energy should be carefully checked when applying the mass scaling.

Profiles with geometric irregularities are generally considered in the wheel-rail impact contact simulations [34–38,43]. One example of the measured rail top surface with geometric irregularities at an insulated rail joint (IRJ) is shown in Fig. 6. The rail surface geometric irregularities measured by Railprof [37] or HandySCAN [72] may be imposed on the originally smooth surface of the model by adjusting the nodal coordinates in the input files of the dynamic analysis solver.

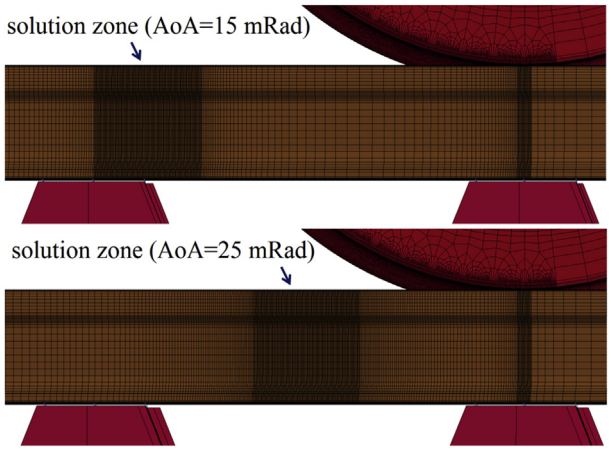

Fig. 5. Remesh rail model to adjust the position of solution zone.

3.1.3. Modeling of other components and model parameters

In addition to the wheel and rail, other train/track components such as the car body, primary suspension, sleepers, fastenings and ballast, may be modeled for different study purposes. The sleepers may also be modeled with hexahedral elements as well as different material properties than those used in the rail and wheel models; the ballast is generally built as spring-damper pairs with a fixed foundation; and the fastening models may significantly influence the track dynamic behavior, whose modeling techniques were comprehensively discussed in Refs. [39,50]. Because the car body and the bogie frame have a negligible influence on high-frequency wheel-rail dynamic interactions [73],

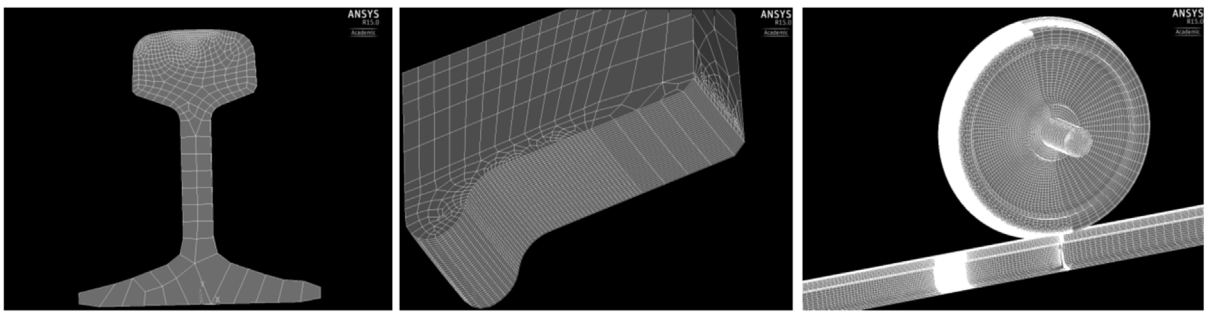

(a) Mesh of rail cross section (b) Mesh of wheel tread (c) Overview of wheel & rail meshes

Fig. 4. Wheel and rail meshes. (a) Mesh of rail cross section (b) Mesh of wheel tread (c) Overview of wheel & rail meshes.

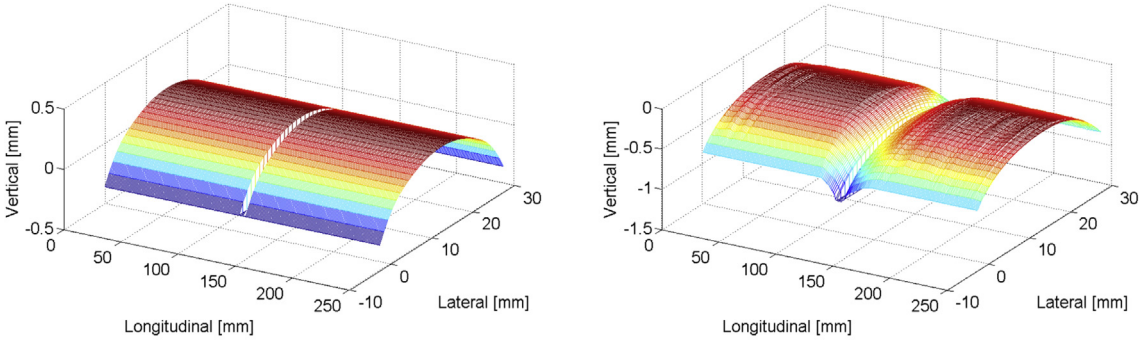

Fig. 6. Measured geometry applied to a wheel-insulated rail joint impact model [31]. (a) Nominal geometry (b) Applying the measured geometry.

they are normally simplified as mass elements connected to the wheelset by the primary suspension with parallel linear springs and viscous dampers.

The explicit FE wheel and rail models generally adopt either elastic or elastoplastic steel with nominal values as the material; and the sleeper models normally adopt elastic timber or concrete as the materials, although inelastic models can be conveniently used. Because the parameters used in fastening and ballast models can rarely be directly measured in the field, they are generally calibrated by fitting the simulated frequency response functions to the measured values [50,51]. Typical values of the parameters employed in the explicit FE wheel-rail interaction models can be found in Refs. [36,37].

3.2. Modeling of static contact

A wheel-rail static equilibrium analysis may be performed to obtain the deformation of structures caused by the gravitational load, which will subsequently be considered the initial conditions for the wheel-rail dynamic interaction analyses. The augmented Lagrangian contact algorithm is recommended for the wheel-rail static contact analysis, which is intrinsically an iterative series of penalty methods with automatic updates of penalty values [74]. The contact pair with a static COF needs to be defined, and it consists of the wheel and rail surface nodes that may be within the static wheel-rail contact patch.

In the wheel-rail static contact analysis, the rail ends, half-wheel-axle ends and car body should be constrained in the lateral (Ux) and longitudinal (Uz) directions. To prevent the wheel model from undesired rolling, its central radial section (normal to the rail longitudinal direction) can be constrained in the longitudinal direction (Uz); see Fig. 7. By applying the gravitational load, the static contact solutions can be obtained. Fig. 8 shows the distribution of the vertical

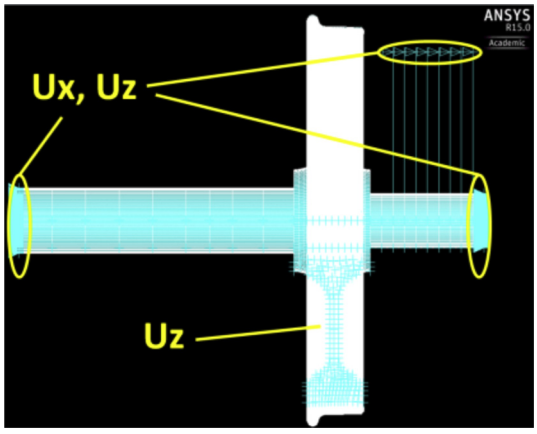

Fig. 7. Displacement constraints.

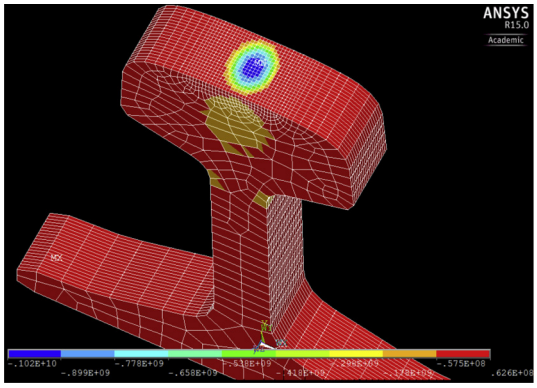

Fig. 8. Static contact solution.

components of the stresses on a piece of rail model that was in contact with the wheel model in a static contact analysis. An elliptic contact patch can be clearly seen at the top of the rail.

3.3. Modeling of dynamic interactions

As indicated by the numerical solution procedure presented in Table 1, definitions of the wheel-rail rolling contact pair, the initial conditions, and the load and displacement boundary conditions are required to proceed with an explicit FE wheel-rail dynamic interaction analysis.

3.3.1. Rolling contact pair

A rolling contact pair needs to be defined in the wheel-rail transient frictional rolling calculation. To employ the penalty contact algorithm introduced in Section 2.6, the master and slave segments of the rolling contact pair defined on the rail top and wheel tread should contain the whole prospective rolling contact region; however, the defined contact regions should be as small as possible to reduce the computation costs caused by contact searching. One example of the contact pair defined for an explicit FE wheel-rail dynamic interaction analysis is shown in Fig. 9. **In LS-DYNA, a three-dimensional 'box' may be defined to reduce the contact-associated computational time** [59]**. Only the elements inside the box are active for contact searching.**

Either constant or variable COFs may be used in wheel-rail rolling simulations. Zhao and Li [26] studied wheel-rail dynamic contact solutions that implemented a velocity-dependent COF and concluded that the velocity-dependent COF may mimic a more realistic contact condition and provide a less regular adhesion-slip distribution pattern compared with the constant COF.

Sections 2.6.1 and 2.6.3 mentioned that the scale factor of the penalty contact stiffness f_{SI} plays an important role in the penalty

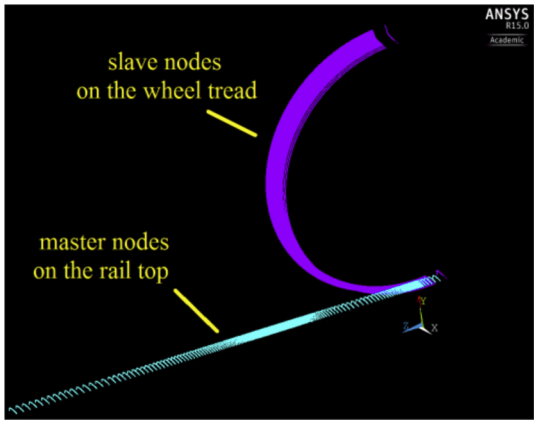

Fig. 9. Contact pair defined for the explicit FE wheel-rail dynamic interaction analysis.

contact algorithm. Ideally, a sufficiently high and low contact stiffness is required so that the penetration and slip distance are acceptably small and the problem can be well-behaved in terms of convergence, respectively. Fig. 10 compares the wheel-rail contact solutions obtained with different scale factors of the penalty contact stiffness: f_{SI} = 1, 0.5 and 0.1. The contact pressure magnitudes are indicated by contour lines, and the tangential stresses are indicated by red arrows. The arrows point in the directions of the tangential stresses, and their lengths are proportional to the magnitude. This figure shows that with decreasing scale factor f_{SI} (from Fig. 10 (a) to (c)), the obtained contact patch areas increases while the contact pressure decreases. A value of f_{SI} = 1 is recommended for wheel-rail dynamic interaction analyses. The contact solutions provided by f_{SI} = 1 are consistent with those obtained by the Hertz contact theory and CONTACT [21,22]; moreover, when applying 1 mm or even finer wheel/rail surface meshes, f_{SI} > 1 may require the time step size to be scaled down for computational stability, which decreases the efficiency of the explicit integration.

3.3.2. Initial conditions

By applying the implicit-explicit sequential analysis, the initial nodal displacements of the wheel-rail transient rolling simulation can be obtained by the wheel-rail static equilibrium analysis illustrated in Section 3.2. The initial nodal velocities of the wheel in both rotation and forward translation should be prescribed, and the value of the applied wheel rotational velocity equals the quotient of the applied translational velocity and the wheel radius. The equivalent translational nodal velocities should also be applied to the primary suspensions and sprung mass because they travel forward together with the wheel.

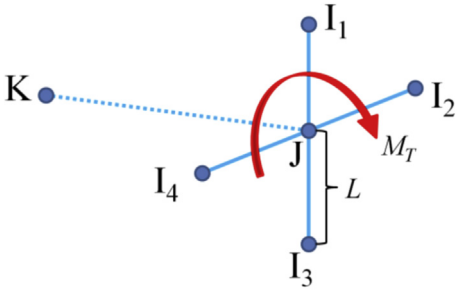

Fig. 11. Driving torque applied to four H-L beam elements.

3.3.3. Load boundary conditions

In addition to the gravitational load illustrated in Section 2.3.1, the driving torque is another widely used load boundary condition in the simulation of wheel-rail tractive frictional contact [34–38,43]. Because the hexahedral elements used to construct wheel models have only translational freedom, the Hughes-Liu (H-L) beam elements [75] degenerated from the hexahedral element can be employed to take the externally exerted torque. As shown schematically in Fig. 11, four H-L beam elements with length L are used. The L value should not be too small because the critical time step size of the H-L beam element for integration stability is $\Delta t_{H-L} = L/\sqrt{E/\rho}$. Each H-L beam element consists of three nodes: I_j (j = 1,2,3,4), J and K. Nodes $I_1 \sim I_4$ and J are all attached to the wheel model and located in the same plane S. Node J is the driven node located at the wheel axial center and shared by the four beam elements. Node K is also shared by the four beam elements, and it is required to define the axis system of beam element. The vector pointing from K to J is normal to plane S. A driving torque M_T in plane S is applied to the driven node J, and its direction is determined by the right-hand rule.

Driven by the torque, the wheel rolls along the rail with a consequently generated longitudinal creep force F_L between the wheel and rail, which satisfies the requirement that the traction coefficient μ_T is less than the COF μ. The traction coefficient is distinguished from the COF in wheel-rail rolling contact studies by its definition in Eqn. (32):

$$\mu_T = \frac{F_L}{F_N} < \mu \tag{32}$$

where F_L and F_N are the longitudinal and normal contact forces, respectively, and μ is the overall COF of the contact pair that limits the traction force transmitted in the contact. The overall COF may be

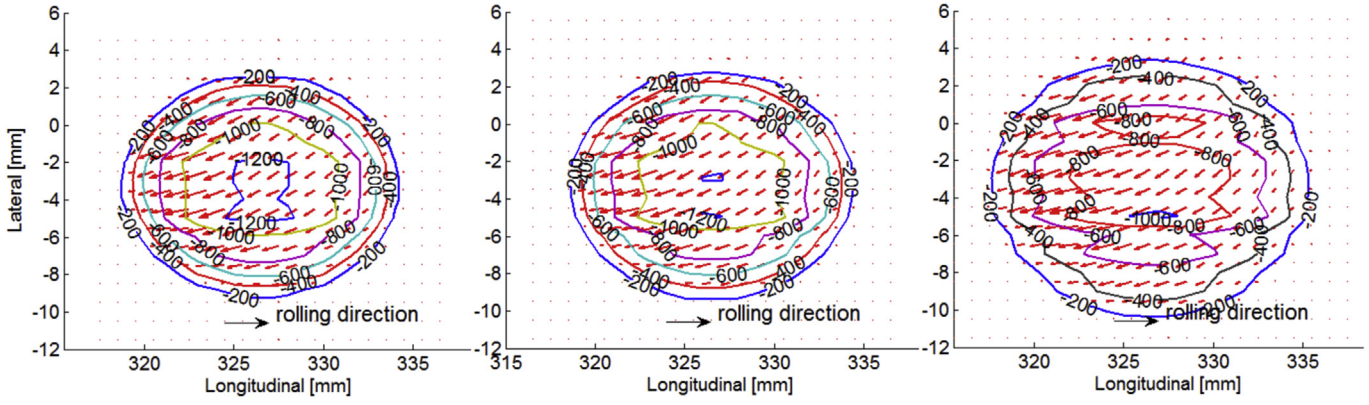

Fig. 10. Contact solutions with different f_{SI} values (contour graph unit: MPa). (a) Contact stress (f_{SI} = 1) (b) Contact stress (f_{SI} = 0.5) (c) Contact stress (f_{SI} = 0.1).

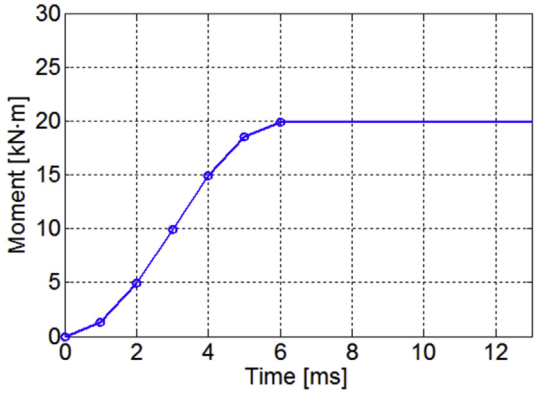

Fig. 12. Functional driving torque.

different from the local COF at certain nodes when the velocity-dependent friction is considered [26]. In addition, the traction coefficient may be assumed to be constant in stationary rolling, whereas it varies with time in dynamic rolling because of vibration, and its nominal value is proportional to the applied driving torque (Eqn. (32)).

A sudden exertion of driving torque may bring significant excitation to the wheel-rail rolling system. A gradually increased driving torque is thus suggested to avoid excitation as much as possible [28] and minimize the dynamic relaxation process (see Section 3.3.5). A functional driving torque $M_T(t)$ is investigated here and is expressed as follows:

$$M_T(t) = \begin{cases} \frac{M_0}{2}\left(1 - cos\left(\frac{\pi t}{t_0}\right)\right), & t < t_0 \\ M_0 \quad , & t \geq t_0 \end{cases} \tag{33}$$

where M_0 is the maximum value of the torque and t_0 is the duration required to reach M_0. Fig. 12 graphically shows the loading function with $M_0 = 20$ kN m and $t_0 = 6$ ms. Fig. 13 compares the calculated wheel-rail normal loads and creep forces with the applications of the loading function in Eqn. (33) and a constant driving torque $M_T(t) = 20$ kN m. This figure shows that the functional driving torque significantly damps the undesired excitation on the creep force, whereas it has less, if any, effect on the normal load.

3.3.4. Displacement boundary conditions

Different displacement boundary conditions may be applied to the explicit FE wheel-rail interaction models according to different research objectives. When the structural dynamics are of less concern or quasi-steady-state contact solutions are desired, the bottom surface of the rail foot may be fully constrained as in the models presented in Refs. [21,22]. When the dynamic effects must be considered and captured, a more detailed modeling of the track substructure is necessary [12,34,35,37,43,47,50,51]. The fastening models simplified as spring-damper pairs may be constrained in the lateral and longitudinal directions if only the vertical dynamics are of concern [51]. More complex boundary conditions are required when solid rail-pad representations of rail fastenings are used [50]. Because the ballast has less influence on the wheel-rail dynamic contact solutions, it is normally constrained in both the lateral and longitudinal directions and fixed at the foundation.

When only a half wheelset is modeled, the inner end of the wheel half-axle can be constrained in the lateral direction to keep the rolling wheel from toppling over. The ends of the finite-length rail models are generally constrained in the lateral and longitudinal directions, which may cause reflective waves that influence the solutions, especially when the track models are insufficiently long. A numerical experiment conducted in Ref. [76] indicated that a FE track model with a length of 20 m is considered sufficiently long to reduce the influence of wave reflection, whereas a length of 10 m may meet engineering requirements for reproducing the measured axle box acceleration. Non-reflective boundary conditions have also been implemented in certain commercial FE programs [59,60], and their application on wheel-rail dynamic interactions is currently under development.

3.3.5. Dynamic relaxation

In the analysis of wheel-rail dynamic interactions, a certain length of rolling distance from the wheel initial position to the solution zone is necessary to damp the oscillations caused by the wheel/rail initial kinematic and potential energy from imperfect static equilibrium [22,77]. This process is called dynamic relaxation. Because the wheel-rail rolling contact physically excites vibrations of the structures and waves in continua, the quasi-steady state may be considered to be achieved by the dynamic relaxation when the oscillations are damped out to less than 10% of the static values [12]. The wheel-rail dynamic interaction solutions obtained after the process of the dynamic relaxation can be output for post-processing.

3.3.6. Time step control

As mentioned in Section 2.2.3, a scale factor sf is employed to control the time step and to guarantee the stability of the explicit integration, and $sf = 0.9$ has been widely used in previous explicit FE wheel-rail interaction studies. Applying smaller time steps in the explicit FEM may produce better accuracy as reported in Ref. [20]. Fig. 14 compares the contact solutions obtained with $sf = 0.9$ and 0.6 (used for explosive problems), where F_n, F_t, and μ are the amplitudes of the contact pressure, surface shear stress, and COF, respectively. The excellent consistency of the results obtained with different value of sf indicates that a scale factor of 0.9 is acceptable for wheel-rail interaction analyses, and it guarantees integration stability and simultaneously decreases the solution time.

4. Solution analyses

The previous section proposes pre-processing knowledge for the explicit FE wheel-rail dynamic interaction analysis; this section introduces post-processing approaches to converting the output of numerical programs for wheel/rail nodal forces and nodal motions into wheel-rail contact and dynamics solutions.

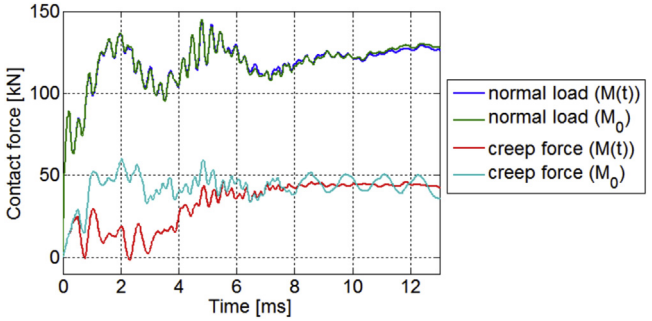

Fig. 13. Forces obtained with different torque functions.

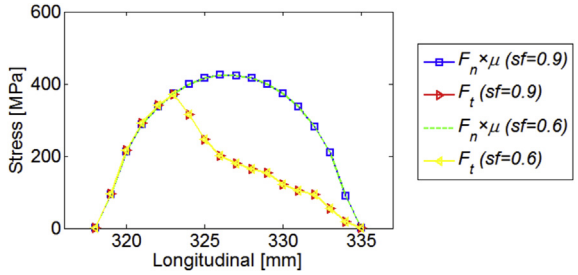

Fig. 14. Comparison of contact stresses calculated with $sf = 0.9$ and 0.6.

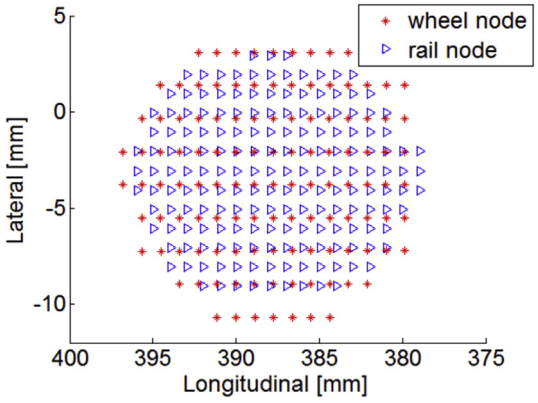

Fig. 15. Wheel and rail nodes in the contact patch

4.1. Contact solutions

The wheel-rail contact solutions of interest generally include the contact patch area, normal and shear contact stresses, and micro-slip and adhesion-slip distributions within the contact patch. These solutions can be obtained by post-processing the nodal force and nodal motion simulated by the wheel-rail dynamic interaction models.

4.1.1. Contact patch area and stresses

The contact patch area may be determined with surface nodal forces: a surface node is in contact if the nodal force in the direction normal to the local surface is non-zero [12,21,22]. Hence, the first step is to convert the output surface nodal forces in the global coordinate system into those in the local coordinate system. Because inertia force is included in the dynamic analyses, the force of a surface node outside the contact may be small but non-zero; thus, a non-zero threshold (e.g., 0.001 N) is used in practice to determine whether a node is in contact. Fig. 15 shows one example of the wheel and rail nodes in contact determined by this rule.

The contact stresses, including the surface normal stress and shear stress, may be calculated with the nodal forces in the local coordinate system. For the generally used quadrilateral segments:

$$\sigma_i^M = \sum_{J=1}^{4} \frac{f_i^{MJ}}{4l^2} \qquad i = 1,2,3 \tag{34}$$

where σ_i^M is the contact stress vector on the *Mth* segment of the wheel/rail surface and the spatial components, with $i = 1,2,3$ representing the normal, lateral and longitudinal directions in the local coordinate system, respectively; f_i^{MJ} is the local nodal force vector, with $J = 1,2,3,4$ representing the number of the nodes constructing segment M as shown schematically in Fig. 16; and l is the dimension of the quadrilateral segment. According to Newton's third law, the contact stresses may be

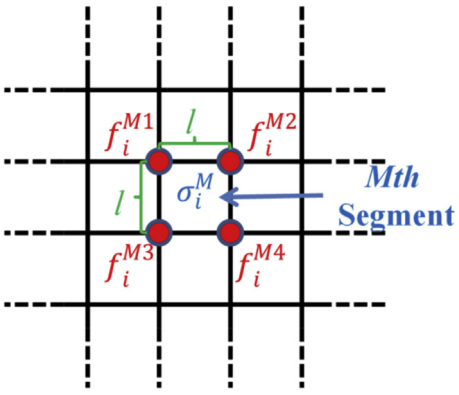

Fig. 16. Nodal forces converted into contact stresses.

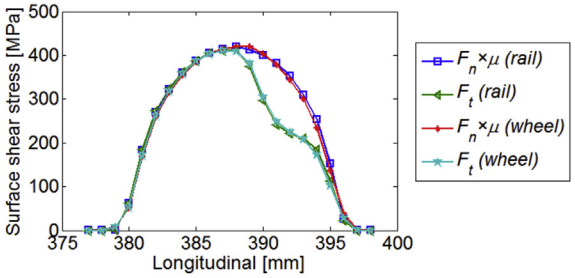

Fig. 17. Contact stresses calculated with the wheel and rail nodal forces.

calculated with either the wheel nodal forces or rail nodal forces. Fig. 17 compares the contact stresses calculated with the wheel and rail nodal forces and indicates that the choice has negligible influence on the calculated contact stresses.

4.1.2. Micro-slip distribution

The micro-slip refers to the tangential relative velocity between two particles in contact. As explained in Section 2.6.1, a rail surface contact node is actually in contact with the "contact point" rather than a wheel surface node; thus, interpolations are required to convert the velocities of wheel nodes into the velocities of the "contact points". Fig. 18 schematically shows a length-weighted linear interpolation scheme. In Fig. 18 (a), the red cross represents an arbitrary rail node N_r and the four blue spots N_{wi} $(i = 1,2,3,4)$ represent the four wheel nodes composed of the wheel surface segment in contact with the rail node N_r. Another blue spot overlapping the red cross in Fig. 18 (b) denotes the interpolated "contact point" N_w on the wheel surface and in contact with rail node N_r; and l_i $(i = 1,2,3,4)$ indicates the distances from the "contact point" N_w to the four sides of the wheel surface contact segment.

We may obtain the interpolated velocities $\boldsymbol{v_w}$ of the "contact point" N_w by the length-weighted linear interpolation as follows:

$$\boldsymbol{v_w} = \frac{l_2 l_4 \boldsymbol{v}_1 + l_1 l_4 \boldsymbol{v}_2 + l_2 l_3 \boldsymbol{v}_3 + l_1 l_3 \boldsymbol{v}_4}{(l_1 + l_2)(l_3 + l_4)} \tag{35}$$

where $\boldsymbol{v}_i (i = 1,2,3,4)$ represents the nodal velocities of the wheel nodes N_{wi}. The micro-slip $\boldsymbol{s_n}$ may then be calculated as follows:

$$\boldsymbol{s_n} = \boldsymbol{v_w} - \boldsymbol{v_r} \tag{36}$$

where $\boldsymbol{v_r}$ are the nodal velocities of the rail node N_r. The length-weighted linear interpolation scheme is also applicable to the calculations for the displacement, acceleration and vertical coordinate (normal to the local contact surface) of the "contact points" on the wheel. The accuracy of the length-weighted linear interpolation scheme may conveniently be estimated by comparing the wheel vertical coordinates before and after interpolation. Fig. 19 shows that the interpolated wheel surface formed by the "contact points" overlaps the original wheel surface, indicating that the interpolation scheme is reliable. In addition, note that the calculated wheel-rail contact patch is not flat but saddle shaped. This result confirms that FEM drops the half-space assumption and the non-flat contact patch may cause geometric spin. The geometric spin calculated with the explicit FEM is discussed in Refs. [21,22].

4.1.3. Adhesion-slip distribution

The division of the adhesion and slip regions in the contact patch is an important feature of the frictional rolling contact. The slip region can be distinguished from the adhesion region either by comparing the surface shear stress F_t with the traction bound $\mu|F_n|$ or by calculating the micro-slip s_n within the contact patch. A node is in a slip region if:

$$\mu|\boldsymbol{F_n}| - |\boldsymbol{F_t}| < \varepsilon_T \qquad or \qquad |\boldsymbol{s_n}| > \varepsilon_s \tag{37}$$

where ε_T and ε_s are the tolerances of the two approaches. A value of

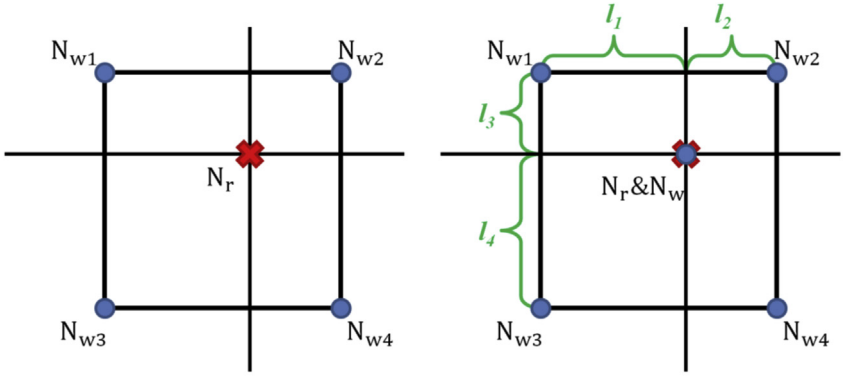

Fig. 18. Interpolated wheel nodal coordinate/motions into rail. (a) Before interpolation (b) After interpolation.

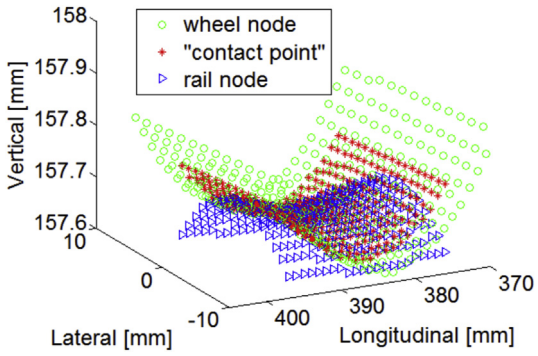

Fig. 19. Coordinates/positions of wheel and rail nodes.

0.3% of the maximal tangential nodal force in the contact patch is suggested for ε_T [21,26,28], whereas a value of 0.05 m/s is suggested for ε_s [26]. For a robust wheel-rail dynamic interaction model, the calculated adhesion-slip distribution determined by both approaches should be consistent with each other.

4.2. Structural dynamics

To obtain the structural dynamic responses, which are generally the vibration acceleration and velocity, the nodes enclosed by the part of the structure of interest need to be selected. The structural vibration accelerations $\ddot{\boldsymbol{u}}_{str}$, for example, may then be calculated by averaging the accelerations of the nodes enclosed by the structural part in the global coordinate system $\ddot{\boldsymbol{u}}^N$:

$$\ddot{\boldsymbol{u}}_{str} = \frac{1}{n}\sum_{N=1}^{n} \ddot{\boldsymbol{u}}^N \tag{38}$$

where n is the total number of nodes enclosed by the structural part. Fig. 20 compares the simulated and measured hammer-excited rail acceleration at different locations along the rail. The legend of each graph indicates the distance from the hammer excitation point to the response location. Each simulation result (red curves) is the average of the accelerations of the nodes in the vicinity (within about 1 cm) of the response location.

5. Numerical example

This section provides a numerical example of simulating wheel-rail impact at a typical IRJ (see Fig. 21). This numerical example demonstrates that the explicit FEM is capable of handling arbitrary contact geometries, nonlinear material properties, and dynamic effects.

To obtain the dynamic contact solutions between a rolling wheel and the target IRJ shown in Fig. 21, we performed three simulations by varying the material and/or geometric parameters of one explicit FE wheel-rail interaction model. Simulation 1 adopted an elastic wheel/rail material and the nominal rail geometry (Fig. 6 (a)); simulation 2 used elastoplastic material and nominal geometries; and simulation 3 used elastoplastic material and the measured IRJ geometry (Fig. 6 (b)). For each simulation, the contact solutions of three consecutive output time steps are displayed in Fig. 22 to show the main characteristics of the wheel-IRJ dynamic interactions.

In Fig. 22 (a) and (b), excluding the discontinuous contact in the middle graphs, the wheel-rail contact solutions obtained with both elastic (simulation 1) and elastoplastic (Simulation 2) models show the same characteristics as those reported in Refs. [22,23]. The contact patches simulated with the elastic model have elliptical shapes, whereas those with the elastoplastic model have “egg” shapes. The amplitudes of the contact pressures are located approximately in the middle of the contact patches for the elastic case but shift forward and are reduced by the plastic deformation for the elastoplastic case. The contact patch areas simulated with the nominal geometry in Fig. 22 (a) and (b) basically remain steady and increase to a small extent during impact, whereas simulation 3 with the measured geometry in Fig. 22 (c) provides much more pronounced non-steady-state contact solutions. In simulation 3, the contact patch shape, which is neither elliptical nor “egg-shaped”, and the pressure distribution vary considerably with time due to the contact geometric irregularities and wheel-rail impact.

In addition, impact wave patterns were produced by the wheel-IRJ dynamic interaction simulations. One example produced by simulation 3 is shown in Fig. 23, which confirms that the explicit FE wheel-rail interaction analysis may take dynamic effects into account.

6. Conclusions and future work

This paper has systematically explored the core algorithms employed in the explicit FE wheel-rail interaction analyses and theoretically demonstrated that the explicit FEM is a suitable approach for solving dynamic frictional rolling contact by fully coupling the calculation of frictional rolling contact with the calculation of high-frequency structural dynamics. An indirect validation method for dynamic contact solutions has been proposed. The reliability of the wheel-rail dynamic interaction solutions can be confirmed by separately verifying the quasi-steady-state contact solutions against Hertz contact theory and CONTACT and validating the structural dynamic responses with measurements. To promote the broad use of the method, this **paper** has also proposed procedures for establishing robust explicit FE wheel-rail dynamic interaction models and converting outputs into solutions of rolling contact and dynamic responses. The summarized algorithms and the proposed procedures can also be applied to the modeling of

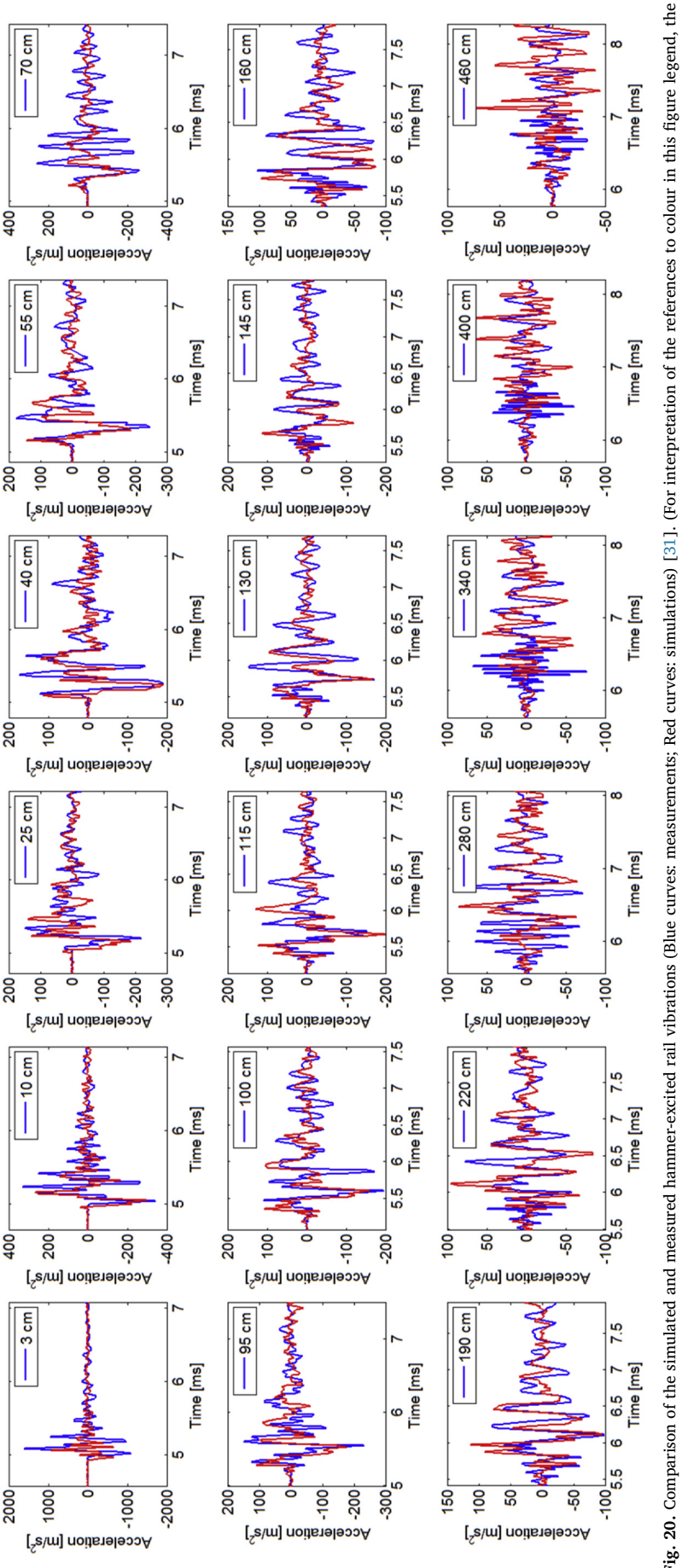

Fig. 20. Comparison of the simulated and measured hammer-excited rail vibrations (Blue curves: measurements; Red curves: simulations) [31]. (For interpretation of the references to colour in this figure legend, the reader is referred to the Web version of this article.)

Fig. 21. Typical IRJ in the Dutch railway network.

dynamic interactions occurring to tire-road, bearings and gears.

The explicit FEM is considered a promising approach to explaining certain enigmas in railway research, such as squeal and corrugation, whose generation mechanisms are closely related to both the wheel-rail frictional rolling and wheel/track dynamic behavior. Future work required for these potential applications may include the following aspects.

- A half wheelset model may not accurately simulate wheel-rail contact when the dynamics of the other half wheelset is not negligible. A full wheelset model considering full dynamics of wheel-rail contact has been presented in Ref. [43] to simulate wheel-turnout contact. A full wheelset model may also be employed in future studies to reliably calculate unstable wheel vibration during curving motions.
- Solid rail-pad representations with proper material parameters proposed in Ref. [50] may be adopted in future studies of wheel-rail dynamic interactions to improve the accuracies of the lateral and longitudinal dynamics simulations.
- Wave phenomena induced by wheel-rail dynamic interactions must be further investigated. Experimental validation of the waves simulated by the proposed explicit FE models should be conducted.

In addition, an explicit FEM solver dedicated to the analysis of wheel-rail dynamic interactions may be developed in the future. The computation cost is expected to be reduced by eliminating redundant conditional statements in the general-purposed explicit FE commercial programs, and the newly developed solver may also provide more convenience and flexibility to amendments to the algorithm. The penalty contact algorithm with nonlinear [78] or functional penalty contact stiffness, the dynamic contact algorithms developed for more sensitive and realistic tangential contact solutions, and the coupling with multibody dynamics analyses may be implemented for future analyses of wheel-rail dynamic interactions.

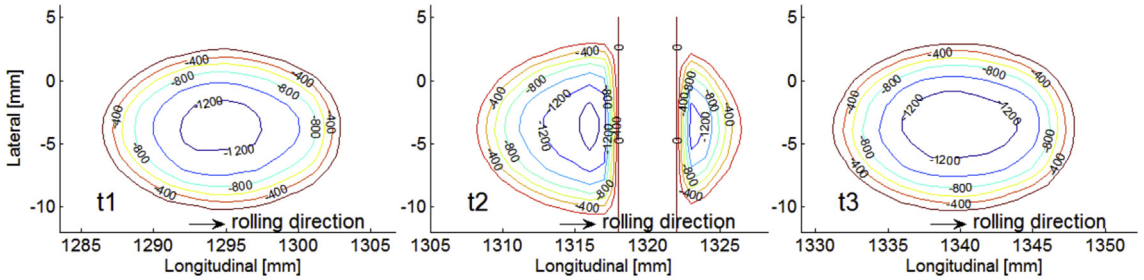

(a) Simulation 1 (elastic material and nominal geometry): elliptical contact patch

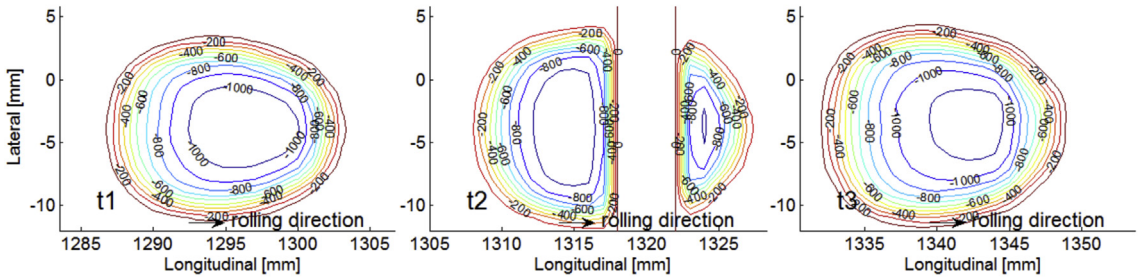

(b) Simulation 2 (elastoplastic material and nominal geometry): “egg-shaped” contact patch

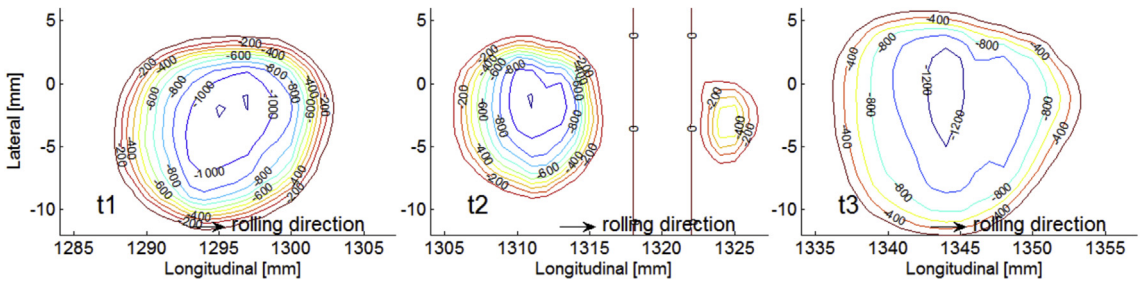

(c) Simulation 3 (elastoplastic material & measured geometry): non-steady-state contact patch

Fig. 22. Evolution of the wheel-rail contact pressure obtained by three different simulations, **(a)** Simulation 1 (elastic material and nominal geometry): elliptical contact patch, **(b)** Simulation 2 (elastoplastic material and nominal geometry): “egg-shaped” contact patch, **(c)** Simulation 3 (elastoplastic material & measured geometry): non-steady-state contact patch.

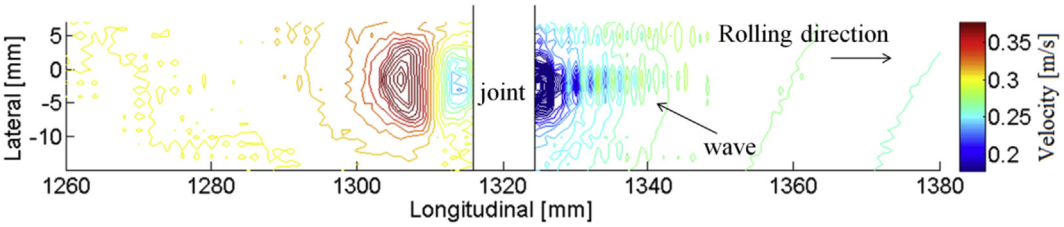

Fig. 23. Impact wave pattern produced by the wheel-IRJ interaction simulation.

Declarations of interest

None.

Acknowledgements

This work was supported by the China Scholarship Council; and the Dutch railway infrastructure manager ProRail.

References

[1] Knothe K, Wille R, Zastrau BW. Advanced contact mechanics–road and rail. Veh Syst Dyn 2001;35:361–407.
[2] Shabana AA, Sany JR. A survey of rail vehicle track simulations and flexible multibody dynamics. Nonlinear Dynam 2001;26:179–210.
[3] Hertz H. Ueber die Berührung fester elastischer Körper. J für die Reine Angewandte Math (Crelle's J) 1882:1882.
[4] Mindlin RD. Compliance of elastic bodies in contact. J Appl Mech 1949:259–68.
[5] Carter FW. On the action of a locomotive driving wheel. P R Soc Lond a-Conta. 1926;112:151–7.
[6] Vermeulen PJ, Johnson KL. Contact of nonspherical elastic bodies transmitting tangential forces. J Appl Mech 1964;31:338.
[7] Damme S, Nackenhorst U, Wetzel A, Zastrau BW. On the numerical analysis of the wheel-rail system in rolling contact. L Not App M 2003;6:155–74.
[8] Nackenhorst U. The ALE-formulation of bodies in rolling contact. Comput Meth Appl Mech Eng 2004;193:4299–322.
[9] Li Z. Wheel-rail rolling contact and its application to wear simulation. Delft University of Technology; 2002.
[10] Kalker JJ. Three-dimensional elastic bodies in rolling contact. 1 ed Springer Netherlands; 1990.
[11] Johnson KL. Contact mechanics. Cambridge university press; 1985.
[12] Yang Z, Li ZL, Dollevoet R. Modelling of non-steady-state transition from single-point to two-point rolling contact. Tribol Int 2016;101:152–63.
[13] Hu G, Wriggers P. On the adaptive finite element method of steady-state rolling contact for hyperelasticity in finite deformations. Comput Meth Appl Mech Eng 2002;191:1333–48.
[14] Telliskivi T, Olofsson U. Wheel–rail wear simulation. Wear 2004;257:1145–53.
[15] Sladkowski A, Sitarz M. Analysis of wheel–rail interaction using FE software. Wear 2005;258:1217–23.
[16] Ekberg A, Sandström J. Numerical study of the mechanical deterioration of insulated rail joints. Proc Inst Mech Eng - Part F J Rail Rapid Transit 2009;223:265–73.
[17] Ringsberg J. Rolling contact fatigue analysis of rails inculding numerical simulations of the rail manufacturing process and repeated wheel-rail contact loads. Int J Fatig 2003;25:547–58.
[18] Wiest M, Kassa E, Daves W, Nielsen JCO, Ossberger H. Assessment of methods for calculating contact pressure in wheel-rail/switch contact. Wear 2008;265:1439–45.
[19] Johansson A, Pålsson B, Ekh M, Nielsen JCO, Ander MKA, Brouzoulis J, et al. Simulation of wheel–rail contact and damage in switches & crossings. Wear 2011;271:472–81.
[20] Wu SR, Gu L. Introduction to the explicit finite element method for nonlinear transient dynamics. Somerset, UNITED STATES: John Wiley & Sons, Incorporated; 2012.
[21] Zhao X, Li ZL. The solution of frictional wheel-rail rolling contact with a 3D transient finite element model: validation and error analysis. Wear 2011;271:444–52.
[22] Deng X, Qian Z, Dollevoet R. Lagrangian explicit finite element modeling for spin-rolling contact. J Tribol 2015;137:041401.
[23] Zhao X, Li ZL. A three-dimensional finite element solution of frictional wheel-rail rolling contact in elasto-plasticity. P I Mech Eng J-J Eng. 2015;229:86–100.
[24] Zhao X, Wen Z, Zhu M, Jin X. A study on high-speed rolling contact between a wheel and a contaminated rail. Veh Syst Dyn 2014;52:1270–87.
[25] Vo KD, Tieu AK, Zhu HT, Kosasih PB. A 3D dynamic model to investigate wheel–rail contact under high and low adhesion. Int J Mech Sci 2014;85:63–75.
[26] Zhao X, Li Z. A solution of transient rolling contact with velocity dependent friction by the explicit finite element method. Eng Comput 2016;33:1033–50.
[27] Naeimi M, Li S, Li Z, Wu J, Petrov RH, Sietsma J, et al. Thermomechanical analysis of the wheel-rail contact using a coupled modelling procedure. Tribol Int 2018;117:250–60.
[28] Wei ZL, Li ZL, Qian ZW, Chen R, Dollevoet R. 3D FE modelling and validation of frictional contact with partial slip in compression-shift-rolling evolution. Int J Rail Transp 2016;4:20–36.
[29] Wen ZF, Jin XS, Zhang WH. Contact-impact stress analysis of rail joint region using the dynamic finite element method. Wear 2005;258:1301–9.
[30] Cai W, Wen ZF, Jin XS, Zhai WM. Dynamic stress analysis of rail joint with height difference defect using finite element method. Eng Fail Anal 2007;14:1488–99.
[31] Yang Z, Boogaard A, Chen R, Dollevoet R, Li Z. Numerical and experimental study of wheel-rail impact vibration and noise generated at an insulated rail joint. Int J Impact Eng 2018;113:29–39.
[32] Yang Z, Boogaard A, Wei Z, Liu J, Dollevoet R, Li Z. Numerical study of wheel-rail impact contact solutions at an insulated rail joint. Int J Mech Sci 2018;138–139:310–22.
[33] Zong N, Dhanasekar M. Sleeper embedded insulated rail joints for minimising the number of modes of failure. Eng Fail Anal 2017;76:27–43.
[34] Li ZL, Zhao X, Dollevoet R, Molodova M. Differential wear and plastic deformation as causes of squat at track local stiffness change combined with other track short defects. Veh Syst Dyn 2008;46:237–46.
[35] Molodova M, Li ZL, Dollevoet R. Axle box acceleration: measurement and simulation for detection of short track defects. Wear 2011;271:349–56.
[36] Zhao X, Li Z, Liu J. Wheel-rail impact and the dynamic forces at discrete supports of rails in the presence of singular rail surface defects. P I Mech Eng F-J Rai. 2012;226:124–39.
[37] Molodova M, Li ZL, Núñez A, Dollevoet R. Validation of a finite element model for axle box acceleration at squats in the high frequency range. Comput Struct 2014;141:84–93.
[38] Yang Z, Li Z, Dollevoet RPBJ. An explicit integration finite element method for impact noise generation at a squat. Notes Numer Fluid Mech 2015;126:63–70.
[39] Zhao X, Li Z, Dollevoet R. Influence of the fastening modeling on the vehicle-track interaction at singular rail surface defects. J Comput Nonlinear Dynam 2014;9:031002.
[40] Li Z, Zhao X, Esveld C, Dollevoet R, Molodova M. An investigation into the causes of squats—correlation analysis and numerical modeling. Wear 2008;265:1349–55.
[41] Wiest M, Daves W, Fischer FD, Ossberger H. Deformation and damage of a crossing nose due to wheel passages. Wear 2008;265:1431–8.
[42] Pletz M, Daves W, Ossberger H. A wheel set/crossing model regarding impact, sliding and deformation-Explicit finite element approach. Wear 2012;294:446–56.
[43] Wei Z, Shen C, Li Z, Dollevoet R. Wheel–rail impact at crossings: relating dynamic frictional contact to degradation. J Comput Nonlinear Dynam 2017;12:041016.
[44] Xin L, Markine VL, Shevtsov IY. Numerical analysis of the dynamic interaction between wheel set and turnout crossing using the explicit finite element method. Veh Syst Dyn 2016;54:301–27.
[45] Wei Z, Núñez A, Boogaard A, Dollevoet R, Li Z. Method for evaluating the performance of railway crossing rails after long-term service. Tribol Int 2018;123:337–48.
[46] Ma Y, Mashal AA, Markine VL. Modelling and experimental validation of dynamic impact in 1:9 railway crossing panel. Tribol Int 2018;118:208–26.
[47] Zhao X, Zhao XG, Liu C, Wen ZF, Jin XS. A study on dynamic stress intensity factors of rail cracks at high speeds by a 3D explicit finite element model of rolling contact. Wear 2016;366:60–70.
[48] Chongyi C, Chengguo W, Ying J. Study on numerical method to predict wheel/rail profile evolution due to wear. Wear 2010;269:167–73.
[49] Vo KD, Zhu HT, Tieu AK, Kosasih PB. FE method to predict damage formation on curved track for various worn status of wheel/rail profiles. Wear 2015;322–323:61–75.
[50] Oregui M, Li Z, Dollevoet R. An investigation into the modeling of railway fastening. Int J Mech Sci 2015;92:1–11.
[51] Oregui M, Li ZL, Dollevoet R. An investigation into the vertical dynamics of tracks with monoblock sleepers with a 3D finite-element model. P I Mech Eng F-J Rai. 2016;230:891–908.
[52] Bathe KJ. Finite element procedures. Prentice Hall; 1996.
[53] Wriggers P. Computational contact mechanics. Springer Berlin Heidelberg; 2006.
[54] Wu SR. A priori error estimates for explicit finite element for linear elasto-dynamics by Galerkin method and central difference method. Comput Meth Appl Mech Eng 2003;192:5329–53.
[55] Hallquist JO, Goudreau GL, Benson DJ. Sliding interfaces with contact-impact in large-scale Lagrangian computations. Comput Meth Appl Mech Eng 1985;51:107–37.
[56] Hughes TJR, Taylor RL, Sackman JL, Curnier A, Kanoknukulchai W. A finite element method for a class of contact-impact problems. Comput Meth Appl Mech Eng 1976;8:249–76.
[57] Oden JT, Pires EB. Algorithms and numerical results for finite element approximations of contact problems with non-classical friction laws. Comput Struct

1984;19:137–47.
[58] Wu SR. A variational principle for dynamic contact with large deformation. Comput Meth Appl Mech Eng 2009;198:2009–15.
[59] Hallquist JO. LS-DYNA theory manual. 2006.
[60] Hibbitt K, Sorensen. ABAQUS/Explicit: user's manual: hibbitt. Karlsson and Sorenson Incorporated; 2001.
[61] Sarl M. Radioss theory manual. Mecalog Sarl; 2005.
[62] Wu SR. Lumped mass matrix in explicit finite element method for transient dynamics of elasticity. Comput Meth Appl Mech Eng 2006;195:5983–94.
[63] Flanagan DP, Belytschko T. A uniform strain hexahedron and quadrilateral with orthogonal hourglass control. Int J Numer Meth Eng 1981;17:679–706.
[64] Attaway SW, Hendrickson BA, Plimpton SJ, Gardner DR, Vaughan CT, Brown KH, et al. A parallel contact detection algorithm for transient solid dynamics simulations using PRONTO3D. Comput Mech 1998;22:143–59.
[65] Courant R, Friedrichs K, Lewy H. On the partial difference equations of mathematical physics. IBM J Res Dev 1967;11:215–34.
[66] Belytschko T, Bindeman LP. Assumed strain stabilization of the eight node hexahedral element. Comput Meth Appl Mech Eng 1993;105:225–60.
[67] Puso MA. A highly efficient enhanced assumed strain physically stabilized hexahedral element. Int J Numer Meth Eng 2000;49:1029–64.
[68] Jabareen M, Rubin MB. A generalized cosserat point element (cpe) for isotropic nonlinear elastic materials including irregular 3-d brick and thin structures. J Mech Mater Struct 2008;3:1465–98.
[69] Poritsky H. Stresses and deflections of cylindrical bodies in contact with application to contact of gears and of locomotive wheels. J. of. Appl. Mech. Trans ASME 1950;17:191–201.
[70] Noh G, Bathe K-J. An explicit time integration scheme for the analysis of wave propagations. Comput Struct 2013;129:178–93.
[71] Pletz M, Daves W, Ossberger H. A wheel passing a crossing nose: dynamic analysis under high axle loads using finite element modelling. Proc Inst Mech Eng - Part F J Rail Rapid Transit 2012;226:603–11.
[72] Wei Z, Núñez A, Li Z, Dollevoet R. Evaluating degradation at railway crossings using axle box acceleration measurements. Sensors 2017;17.
[73] Baeza L, Roda A, Carballeira J, Giner E. Railway train-track dynamics for wheelflats with improved contact models. Nonlinear Dynam 2006;45:385–97.
[74] Mijar AR, Arora JS. An augmented Lagrangian optimization method for contact analysis problems, 1: formulation and algorithm. Struct Multidiscip Optim 2004;28.
[75] Hughes TJR, Liu WK. Nonlinear finite element analysis of shells-part II. two-dimensional shells. Comput Meth Appl Mech Eng 1981;27:167–81.
[76] Molodova M. Detection of early squats by axle box acceleration. Delft University of Technology; 2013.
[77] Li S, Li Z, Núñez A, Dollevoet R. New insights into the short pitch corrugation enigma based on 3d-FE coupled dynamic vehicle-track modeling of frictional rolling contact. Appl Sci 2017;7:807.
[78] Ju SH. A frictional contact finite element for wheel/rail dynamic simulations. Nonlinear Dynam 2016;85:365–74.